ChemComm

Recent developments in oxide ion conductors: focusing on Dion–Jacobson phases

Journal:	*ChemComm*
Manuscript ID	CC-FEA-09-2022-005288.R1
Article Type:	Feature Article

ARTICLE

Recent developments in oxide ion conductors: focusing on Dion–Jacobson phases

Received 00th January 20xx,
Accepted 00th January 20xx

DOI: 10.1039/x0xx00000x

Wenrui Zhang and Masatomo Yashima*

Oxide-ion conductors, also known as "oxygen ion conductors," have garnered significant attention in recent years due to their extensive applications in a variety of electrochemical devices, including oxygen concentrators, solid-oxide fuel cells (SOFCs), and solid oxide electrolysis cells. The key to improving the performance of these devices is the creation of novel oxide-ion conductors. In this feature article, we discuss the recent developments of new structural families of oxide-ion conductors and of the Dion–Jacobson-type layered oxide-ion conductors with a particular emphasis on $CsM_2Ti_2NbO_{10-\delta}$ (M = Bi and lanthanoids; δ represents oxygen-vacancy content) and their solid solutions. $CsBi_2Ti_2NbO_{10-\delta}$ is the first example of an oxide-ion conductor with a Dion–Jacobson-type layered perovskite structure, and the structural characteristics of these materials are extracted here. We have proposed an original concept that the large sized Cs^+ cations and M^{3+} displacements yield the large bottlenecks for oxide-ion migration, which would facilitate the discovery of novel oxide-ion conductors. This article presents evidence that Dion–Jacobson-type layered perovskites are superior oxide-ion conductors. We also demonstrate how the information gleaned from these studies can be applied to the design of novel oxide-ion conductors.

1. Introduction

1.1 Oxide-ion conductors

Oxide-ion conduction in solids was discovered by Nernst over a century ago.[1] Oxide-ion conductors, also known as "oxygen-ion conductors" or "oxide-ion conducting materials," have attracted significant interest due to their wide applications in energy, environmental, and biomedical fields, such as solid-oxide fuel cells (SOFCs), solid oxide electrolysis cells (SOECs), oxygen sensors, oxygen concentrators, and catalysts.[2,3,4,5,6,7,8,9,10,11]

In solids, oxide ions generally migrate via vacancy or interstitial mechanisms. High oxide-ion conductivities have been reported for a limited number of structural families.[12,13,14,15,16,17] Since the limited structural families restrict their further development, the discovery of new structural families of oxide-ion conductors is crucial for the development of these applications.[18,19,20,21,22,23,24] Meanwhile, improvement of oxide-ion conductivity requires a thorough understanding of the oxide-ion diffusion paths and conduction mechanisms at the atomic level.[25,26,27,28,29,30] Consequently, a thorough study of the diffusion paths and conduction mechanisms in new oxide-ion conductors is of equal importance and must be specifically investigated.

1.2 Fluorite-type and pyrochlore-type oxides and their related oxides

Oxide-ion conduction has been observed in numerous structural families. In recent years, Yttria-stabilized zirconia (YSZ), scandia-stabilized zirconia, calcia-stabilized zirconia, and ceria-zirconia have been the most studied oxide-ion conductors, and YSZ is used as electrolyte materials in commercial SOFCs.[31,32,33,34,35] They crystallize into fluorite-type or distorted fluorite-type structures and exhibit high oxide-ion conductivities at elevated temperatures due to their high oxygen vacancy concentrations.[36] Possible oxide-ion diffusion pathways in the tetragonal ceria-zirconia material were visualized using nanocrystalline $Ce_{0.5}Zr_{0.5}O_2$, revealing curved pathways along the fluorite <100> and <110> directions that form a three-dimensional (3D) network (**Fig. 1**).[37] Similar with many cubic fluorite-structured materials, the curved pathways of O_a–O_b and O_c–O_d paths along the <001> direction are observed in $Ce_{0.5}Zr_{0.5}O_2$. Moreover, the O_a–O_c and O_b–O_d paths along the $<110>_F$ direction are also the possible diffusional pathways. But the paths of O_a-O_d and O_b-O_c along the $<111>_F$ direction are not allowed because the oxide ions are not stable around the center of the path.[37] In particular, YSZ has excellent physicochemical stability in oxidized and reduced environments, as well as for long-term operation. However, the high operating temperature of YSZ, usually higher than 800 °C, limits its further practical applications.[38] Gadolinia-doped ceria (GDC) has significantly higher oxide-ion conductivities than YSZ (~0.3 Scm^{-1} at 900 °C [Ref.[39]]), as well as at low and intermediate temperatures (300–600 °C). Despite the high oxide-ion conductivities, GDC demonstrates poor stability at low oxygen partial pressures (pO_2), where pO_2 is less than 10^{-5} atm. In fact, Ce^{4+} can be reduced to Ce^{3+} at low pO_2, resulting in n-type electronic conduction in the system.[40]

Department of Chemistry, School of Science, Tokyo Institute of Technology, 2–12–1 W4–17 O-okayama, Meguro-ku, Tokyo, 152–8551, Japan

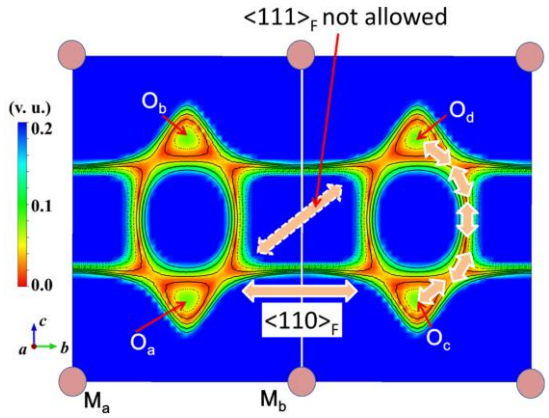

Fig. 1 Difference bond valence sum (DBVS) map for an oxide ion, in two unit-cells of the nanocrystalline $Ce_{0.5}Zr_{0.5}O_2$ at 1023 K. The $<hkl>_F$ denotes the set of all directions that are equivalent to [*hkl*] by symmetry, where the subscript F denotes the pseudo fluorite lattice. Copyright © 2012 American Chemical Society.[37]

Bismuth oxide and its derivatives exhibit very high oxide-ion conductivities of ~1 Scm^{-1} at 729 °C.[41] Bismuth oxide and its solid solutions exhibit a complicated positional disorder of oxide ions that spread over a large area and shift to the <111> directions from the ideal fluorite 8*c* site (**Fig. 2**).[42,43] The presence of oxygen vacancies, high polarizability of the Bi^{3+} cations, and the lone pair of Bi^{3+} can explain the high conductivities.[44,45,46] δ-Bi_2O_3, a high-temperature cubic fluorite-type bismuth oxide, exhibits the highest oxide-ion conductivities through oxygen vacancies. By partially substituting Bi^{3+} with other cations, the high-temperature δ-Bi_2O_3 phase can be stabilized at lower temperatures.[47] However, these electrolytes are unstable under reducing conditions, as evidenced by the reduction of Bi^{3+} and the degradation of conductivity during 500-h-long tests at 500 °C.[45,48,49,50]

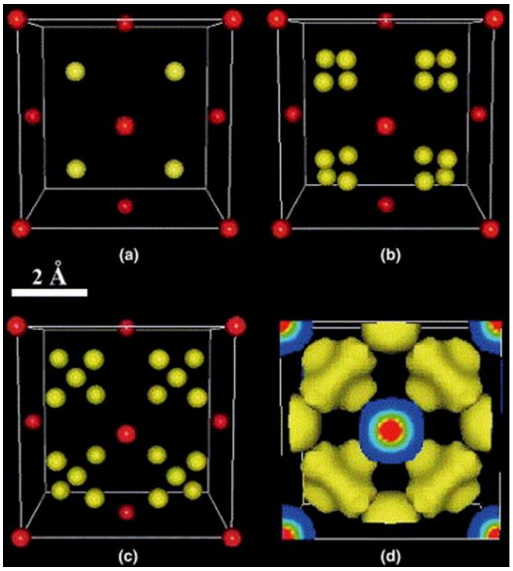

Fig. 2 Structural models for δ-Bi_2O_3. (a) Gattow model based on an ideal fluorite-type structure: average distribution of six oxygen atoms at the site (8*c*) of *Fm*-3*m* (*xxx*, *x* = 1/4); (b) Harwig model: average distribution of six oxygen atoms at the site (32*f*) of *Fm*-3*m* (*xxx*, *x* = 1/4+δ); (c) Battle model: six oxygen atoms are distributed at the 8*c* and 32*f* sites; and (d) scattering amplitude distribution of δ-Bi_2O_3 at 778 °C. Copyright © 2003 Elsevier B.V.[42]

The pyrochlore-type oxide-ion conductors, such as $Gd_2Ti_2O_7$ and $Gd_2Zr_2O_7$, have the formula $A_2B_2O_7$ and crystal structures in which the *A* and *B* cations are arranged along the [110] directions, where the [*hkl*] denotes the direction index of the lattice.[51,52,53] The combined technique of high-temperature neutron diffraction and maximum-entropy method (MEM) was used to visualize oxide-ion diffusion paths in the pyrochlore-type oxide-ion conductor $Yb_2Ti_2O_7$, and it was discovered that there are two types of oxide-ion diffusion paths along the <110> and <100> directions (**Fig. 3**).[54] The pyrochlore-type structure can be viewed as a vacancy-ordered fluorite-type structure.[55] Experiments revealed that a cation-disordered defect fluorite structure forms at equilibrium when cations are similar in size, which is governed by the thermodynamics of disordering and the energetics of defect formation.[56] The average structure demonstrates that the order-disorder transformation involves antisite defects, in which *A* and *B* site cations randomly exchange positions and anion Frenkel pairs lead to randomized oxygen vacancies. The local structure is claimed to consist of randomly arranged orthorhombic weberite-type domains.[57] Molecular dynamics has been calculated to quantify the defect states and oxide-ion migration mechanism in pyrochlore-type $Y_2Ti_2O_7$. Defect states have been classified into three types: a Frenkel pair, a single vacancy, and a split vacancy. At low temperatures, most favorable defect type is a split vacancy while at high temperatures, split and single vacancies are found to be equally favorable. Oxide-ion migration occurs by a two-step cooperative mechanism via the split vacancy.[58] Recent neutron total-scattering experiments by Kennedy et al. quantified the relationship between the disorder of oxide ions and Frenkel defects in the pyrochlore phases $Y_2Sn_{2-x}Zr_xO_7$. Substituting Zr for Sn at position 48*f* site distorts the structure and leads to the formation of vacancies that facilitate oxygen diffusion. They asserted that the local structure of the $Y_2Zr_2O_7$ defect fluorite does not contain ordered weberite-type domains, which contradicts a growing number of recent studies that support the weberite-type model.[59] They collected neutron data at low temperatures, which can minimize dynamic thermal disordering.

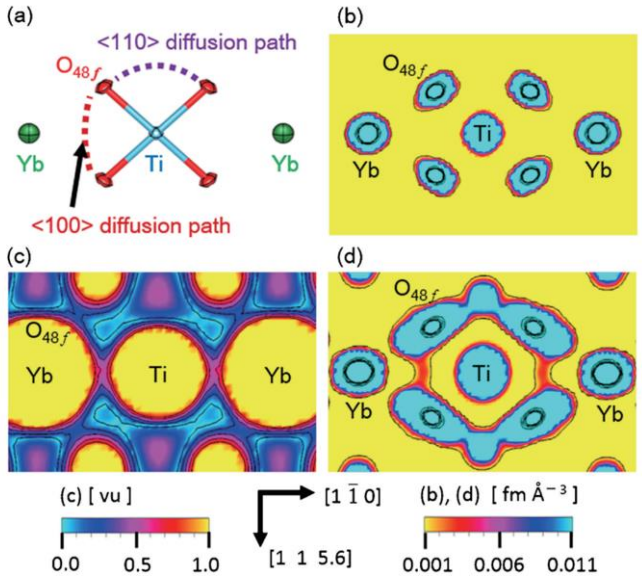

Fig. 3 (a) Part of the refined crystal structure of $Yb_2Ti_2O_7$ at 900 °C. Neutron scattering length density distributions of $Yb_2Ti_2O_7$ at 20 °C (b) and 900 °C (d). (c) Difference bond valence sum (DBVS) map for an oxide ion of $Yb_2Ti_2O_7$, which was calculated for the refined crystal structure using the neutron data taken at 900 °C. O_{48f} denotes an oxygen atom at the 48*f* site. Thermal ellipsoids in panel (a) are drawn at 50% probability level. Contour lines in panels (b) and (d): 0.001–50.001 fm Å^{-3} by 10 fm Å^{-3} steps. Contour lines in the panel (c): 0.0–1.0 vu by 0.2 vu steps. Copyright © 2018 The Ceramic Society of Japan.[54]

1.3 Melilite-type oxide-ion conductors

It has been reported that $LaSrGa_3O_7$-based oxides with the melilite-type structure exhibit high oxide-ion conductivities (~0.1 Scm^{-1} at 900 °C for $La_{1.54}Sr_{0.46}Ga_3O_{7.27}$).[17,60,61] $LaSrGa_3O_7$ possesses a typical gallate melilite structure, consisting alternately of Ga_3O_7 tetrahedral layers and $(La/Sr)_2$ layers along the *c* axis. The La and Sr cations occupy identical positions in the tunnels' fivefold configuration. The stoichiometric $LaSrGa_3O_7$ is an insulator, but by varying the La/Sr ratio, excess oxygen atoms can be introduced into the structure, resulting in high oxide-ion conduction. Although oxygen vacancies are the primary charge carriers in the majority of oxide-ion conducting materials, interstitial oxygen atoms also function as carriers in certain isolated polyhedral anion structures.[17] $La_{1.54}Sr_{0.46}Ga_3O_{7.27}$ can stabilize interstitial oxygen atoms in the network, resulting in an oxide-ion conductivity of 0.02 Scm^{-1} at 600 °C.[17] The interstitial oxygen atoms coordinate with the Ga atoms in the first coordination shell, resulting in the formation of GaO_5 units and distorting the pentagonal rings.[60] According to Tealdi et al., oxide-ion conduction in melilite-type $La_{1.54}Sr_{0.46}Ga_3O_{7.27}$ occurs via a "interstitialcy" or cooperative-type mechanism, which involves the concerted knock-on motion of interstitial and lattice oxygen atoms.[60] Oxide ions in $La_{1.54}Sr_{0.46}Ga_3O_{7.27}$ diffuse anisotropically within the layers of corner-sharing GaO_4 and the rotation of GaO_5 units also aids in the migration of oxide ions. Recently, Schuett et al. investigated the site and migration energies of oxygen interstitials and vacancies in melilite-type $La_{1+x}Sr_{1-x}Ga_3O_{7+x/2}$ using density functional theory (DFT) and Kinetic Monte Carlo simulations. They proved that the macroscopic activation energy is determined by the interaction of the interstitials with the local cation and anion environments. The interstitials in La-rich compositions mostly occupy positions in the center of the pentagonal GaO_4 rings with some off-centered positions, and the oxide ions migrate via the interstitialcy mechanism and the jump between the adjacent rings.[62] Recent evidence of the versatility of melilite oxides includes the oxygen-deficient melilite oxides $Sr_{2-x}Na_xMgSi_2O_{7-0.5x}$, which exhibit a high oxide-ion conductivity of 0.05 Scm^{-1} at 750 °C when x = 0.4.[63] $La_{1+x}Ca_{1-x}Al_3O_{7+0.5x}$ aluminates, a new family of Ga-free melilite-type oxide-ion conductors, exhibit multiple interstitial defect positions in the melilite pentagonal rings, resulting in a variety of local structures surrounding the oxygen interstitial defects.[64] Molecular dynamics simulations have been performed on metastable $La_2Ga_3O_{7.5}$ melilite ceramics, which identified one dimensional diffusion paths of interstitial oxide ion. The interstitial oxide ions migrate from the pentagonal ring containing GaO_5 pyramid unit to its neighboring pentagonal ring mainly along *a* axis through a synergic mechanism.[58] The flexibility of the melilite structure demonstrates the vast potential of these systems, which must be investigated further. At intermediate temperatures, the stability and high oxide-ion conductivities of melilite-type oxide-ion conductors at intermediate temperature are likely to provide potential applications in SOFCs at intermediate temperatures.[17,60,61]

Yasui et al. discovered $Ca_3Ga_4O_9$, a new structure family of oxide-ion conductors.[27] $Ca_3Ga_4O_9$ has a similar structure to the oxide of the melilite type, as both possess a two-dimensional (2D) GaO_4 tetrahedral network in their crystal structures. In the GaO_4 tetrahedral layer, $LaSrGa_3O_7$ melilite has only five-membered rings, whereas $Ca_3Ga_4O_9$ has four- and five-membered rings.[27] The bond valence-based energy landscapes of $Ca_3Ga_4O_9$ suggest that oxide ions migrate in the corner-sharing tetrahedral GaO_4 network through an interstitialcy diffusion mechanism, similar to that of melilite-type conductors.

1.4 Apatite-type oxide-ion conductors

Due to their high conductivities and the flexibility of the apatite structure, apatite-type oxide-ion conductors have garnered considerable interest.[65,66,67] Lanthanum silicates and germanates are the most extensively studied apatite-type oxide-ion conductors, with high conductivities of ~3 × 10^{-3} Scm^{-1} at 700 °C for $La_{9.33}(SiO_4)_6O_2$ and ~3 × 10^{-3} Scm^{-1} at 500 °C for $La_{9.33}(GeO_4)_6O_2$.[68,65,69] The majority of apatite-type oxide-ion conductors have hexagonal symmetry; their structures are composed of isolated SiO_4 or GeO_4 tetrahedra and La cations located at 9 and 7 coordinate sites, respectively.[66] Using high-temperature neutron diffraction and MEM, Yashima et al. discovered two migration pathways in the apatite-type oxide-ion conductor $La_{9.69}(Si_{5.70}Mg_{0.30})O_{26.24}$. One diffusion path of O4—O4 is linear and parallel to the *c* axis, whereas the path of

O3—O5—O4—O5—O3 is perpendicular to the *c* axis (**Fig. 4**).[70,71] In common oxide-ion conductors, oxide ions migrate via oxygen vacancies, such as in perovskite-type and fluorite-type oxide-ion conductors.[68] Several studies have suggested that interstitial oxygen atoms play an important role in the oxide-ion conduction, thereby enhancing the motion of oxide ions through the channels.[72] In contrast, Fujii et al.[65] revealed the presence of Si vacancies □ rather than interstitial oxide ions in La-rich $La_{9.565}$ $(Si_{5.826}□_{0.174})O_{26}$ through experimental analyses and theoretical calculations. Oxide ions migrate predominantly along the c axis, which is a significant factor in the high oxide-ion conductivity of $La_{9.565}(Si_{5.826}□_{0.174})O_{26}$. A highly *c*-axis-oriented apatite-type lanthanum silicate $La_{9.7}Si_{5.3}B_{0.7}O_{26.2}$ polycrystal can be produced through a vapor-solid reaction. Its oxide-ion conductivity is 190 times higher than that of YSZ, which reaches 16 $mScm^{-1}$ at 405 °C.[73] The high oxide-ion conductivity may be attributable to the formation of oxygen vacancies at the O4 site by B doping.[73] The main limitation of these apatite materials is their high sintering temperature (1500–1700 °C), which is hampered by the volatility of Ge and B atoms at high temperatures. Molecular dynamics simulations study were performed on apatite-type $La_{10-x}Bi_xGe_6O_{27}$ (x = 0, 2, and 4), and showed that doping with the lone pair cation can increases the overall mobility of oxygen, corroborating experimental results.[74] Various cation dopants can enhance the sintering capability of apatite systems, and germanium loss can be avoided by employing low-temperature synthesis techniques, such as the sol-gel method and molten-salt synthesis.[66]

Various compounds possessing tetrahedral moieties have been reported to show high oxide-ion conductivities. Except the melilite-type and apatite-type families as we mentioned above, the scheelite-type oxide-ion conductors have also been widely investigated.[75,76,77] For example, the lanthanide cation doped $Pb_{1-x}Ln_xWO_{4+x/2}$ oxides show high oxide-ion conduction thanks to the introduction of interstitial oxide ions ($4.2×10^{-2}$ S cm^{-1} at 800 °C for doped $Pb_{0.8}La_{0.2}WO_{4.1}$).[75]

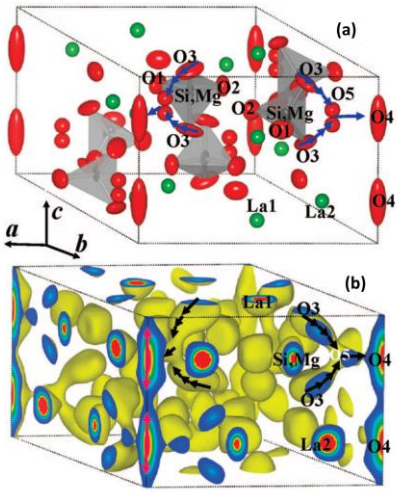

Fig. 4 Refined crystal structure of $La_{9.69}(Si_{5.70}Mg_{0.30})O_{26.24}$ at 1558 °C (a). Oxygen atoms (O3) that are members of the $(Si_{0.95}Mg_{0.05})O_4$ tetrahedron migrate to the oxygen atoms (O4) located at the hexagonal axis through the interstitial oxygen (O5) following a curved path (black arrows). (b) Equicontour surface of the neutron scattering length density distribution. Red arrows indicate a direct linear diffusion pathway of the oxide ions. Copyright © 2008 American Chemical Society.[70]

1.5 LAMOX family of oxide-ion conductors

Lanthanum molybdate $La_2Mo_2O_9$, also known as LAMOX, possesses oxide-ion conductivities comparable to those of YSZ (0.06 Scm^{-1} at 800 °C).[78] $La_2Mo_2O_9$ has two polymorphs of monoclinic α-phase at low temperature and cubic β-phase above 580 °C (oxide-ion conducting phase).[78] The oxygen atoms in the β-phase are distributed at three sites: fully occupied O1 and partially occupied O2 and O3 sites. The partially occupied O2 and O3 sites lead to disordered oxygen distribution around the Mo atoms in the cubic phase, which corresponds to a well-defined short-range structure in the monoclinic phase. According to reports, the high oxide-ion conductivities observed in β-LAMOX are aided by disordered networks, which create favorable migration paths for the oxide ions. The partially vacant sites in β-LAMOX with short inter-site distances suggest a most likely three-dimensional conduction path (**Fig. 5**).[79] However, β-LAMOX exhibits a nonlinear trend of the conductivities in the temperature range of 400 to 450 °C. This behavior can be explained by a phase transition. A recent study found that doping Sr and W at the La and Mo sites, respectively, can stabilize cubic β-LAMOX at room temperature.[80] Meanwhile, LAMOX materials exhibit problems of structural and electrochemical stability at low pO_2 due to the ease of reduction of Mo^{6+} to Mo^{4+} and the ensuing loss of oxygen, which generates n-type electronic conductivities.[75]

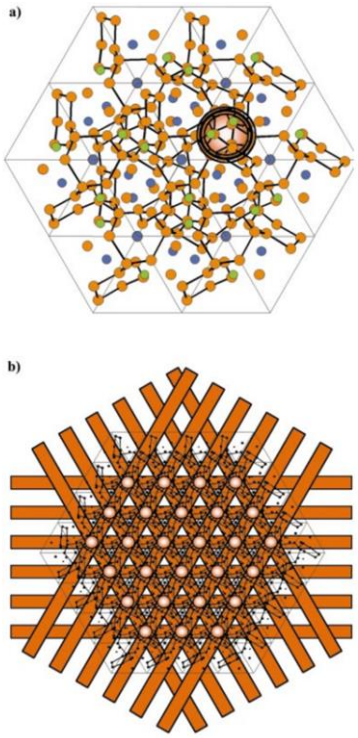

Fig. 5 Conduction path in $La_2Mo_2O_9$: (a) 3D lattice of short O2- and O3- distances in β-LAMOX forming infinite diffusion paths along the [111] cubic direction (direction of the projection). Orange = oxygen, blue = lanthanum, green = molybdenum; and (b) 3D lattice of the conduction paths schematised as infinite cylindrical rods along the cube diagonals. Copyright © 2001 The Royal Society of Chemistry.[79]

1.6 Perovskite-type oxide-ion conductors

The perovskite and its related compounds are a large structural family with a crystal structure similar to the perovskite mineral, calcium titanate $CaTiO_3$. In an ideal ABO_3 perovskite structure, the smaller *B* cations are in 6-coordinated sites that form a BO_6 octahedron, whereas the interstitial voids are occupied by larger *A* cations in a 12-fold coordination. Distortion can be caused by the tilting of BO_6 octahedra and cation displacements, resulting in ~~fewer~~ lower symmetries. A way to rationalize this phenomenon is the use of the tolerance factor *t*,

$$t = \frac{r_A + r_0}{\sqrt{2}(r_B + r_0)},$$

where r_A, r_B, and r_O are the ionic radii of the different species as mentioned above. For instance, when the radius of *A* cation is quite small, resulting in a small *t*, the empty space is filled by tilting the BO_6 octahedra, thereby generating systems with lower symmetries, such as tetragonal, orthorhombic, rhombohedral, and monoclinic systems. Multiple cations can be encapsulated within the structure, allowing for a spectrum of physical and chemical properties.[81,82,83,84,85,86] There are additional perovskite-related structures in addition to the ABO_3 perovskite-type structure, including the layered and hexagonal perovskite structures. High oxide-ion conductivities are exhibited by cubic perovskite oxides, such as doped lanthanum gallates and sodium bismuth titanites. For instance, the conductivities of $La_{0.9}Sr_{0.1}Ga_{0.9}Mg_{0.1}O_{2.9}$ are 0.15 Scm^{-1} at 800 °C and 0.01 Scm^{-1} at 600 °C for $Na_{0.5}Bi_{0.49}Ti_{0.98}Mg_{0.02}O_{2.965}$, respectively.[87,88] In the cubic ABO_3 perovskite oxide-ion conductors, oxide ions migrate along the edge of the BO_6 octahedron via a curved diffusion pathway.[89,90,91,92,93]

Lanthanum gallates are a typical example of perovskite-type oxide-ion conductors ($LaGaO_3$ solid solutions).[21,94,95] Doping $LaGaO_3$ with strontium at the lanthanum site and magnesium at the gallium site results inLa_{1-x} Sr_xGa_{1-y} $Mg_yO_{3-\delta}$ solid solutions (LSGM)with high oxide-ion conductivities (e.g., ~0.15 Scm^{-1} at 800 °C for $La_{0.9}Sr_{0.1}Ga_{0.9}Mg_{0.1}O_{2.9}$). Above 150 °C, the mother phase $LaGaO_3$ crystallizes in the orthorhombic phase and undergoes a phase transition to the rhombohedral phase. Doped compounds exhibit monoclinic, orthorhombic, and cubic phases, depending on the dopants and their concentrations at room temperature.[96] The oxygen vacancies created by the partial substitution of La^{3+} and Ga^{3+} cations with acceptor dopants such as Sr^{2+} and Mg^{2}+ are the key to the high oxide-ion conductivities. Oxide ions diffuse via oxygen vacancies through the edges of the GaO6 octahedra, forming a 3D network of curved diffusion paths, according to calculations and experiments.[94,95,97] $La_{0.4}Ba_{0.6}CoO_{3-\delta}$, a perovskite-type mixed ionic-electronic conductor (MIEC), also exhibits experimental evidence for a curved 3D diffusion pathway. Oxide ions in $La_{0.4}Ba_{0.6}CoO_{3-\delta}$ migrate in the ⟨100⟩ direction close to the stable position and in the ⟨100⟩ direction near the center of the path (**Fig. 6**).[91] Recent research indicates that the 3D curved paths are also a result of the driving force to maximize the electronic interactions of the *B* cation with surrounding oxide ions along the entire migration pathway.[98] Despite the high oxide-ion conductivity of LSGM compounds, the formation of secondary phases such as $LaSrGa_3O_7$ and $LaSrGaO_4$ at the interface of the anode and electrolyte in LSGM-based SOFCs significantly increases the internal ohmic resistance of the cells, decreases the open cell voltage, and consequently degrades the SOFC performance.[99]

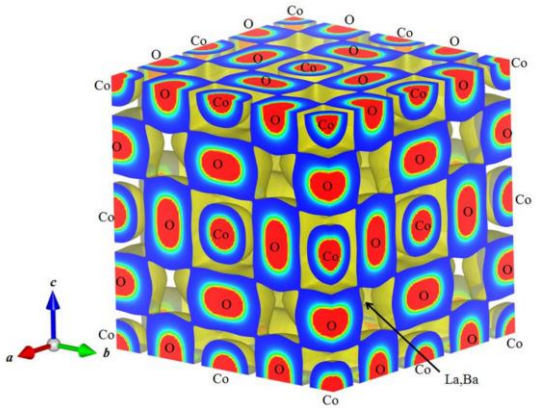

Fig. 6 Three-dimensional network of the oxygen diffusion path of 2 × 2 × 2 unit-cells in $La_{0.4}Ba_{0.6}CoO_{3-\delta}$ at 1227.3 °C. Copyright © 2012 American Chemical Society.[91]

$Na_{0.5}Bi_{0.5}TiO_3$ (NBT), which is well-known as a ferroelectric compound, is another example of an oxide-ion conductor of the cubic perovskite type.[88] Recently, the electrical properties of NBT were reported, and its solid solutions have been extensively studied.[88,100,101,102,103] According to a recent study, the optimal space group for the room temperature phase of NBT-based ceramics is monoclinic *Cc*.[103] During sample preparation at high temperatures, bismuth in the NBT compounds is lost, resulting in Bi-deficient compositions with high oxide-ion bulk conductivities (~1×10^{-3} S cm^{-1} at 500 °C).[88] The deficiency and volatilisation of Bi species in material processing introduce oxygen vacancies, which are responsible for the high oxide-ion conductivities. In contrast, when the atomic ratio of Bi/Na >1, insulating materials are produced.[100] Due to the weaker Bi-O bond, these oxygen vacancies form preferentially in the vicinity of Bi atoms, according to theoretical calculations. Similar to other perovskite-type oxide-ion conductors, the oxide ions migrate through the edges of TiO^6 octahedra. The high polarizability of the Bi atoms, complexity of the NBT lattice, and oxygen vacancies are thought to play the most important roles in oxide-ion conduction.[88] The oxide-ion conductivities are further increased by doping Mg on the Ti site (*B* site), by increasing the oxygen vacancies (e.g., bulk conductivity of ~0.01 Scm^{-1} at 600 °C for $Na_{0.5}Bi_{0.49}Ti_{0.98}Mg_{0.02}O_{2.965}$ [Ref.[88]], and *A*-site doping is another effective method of increasing the ionic conductivity (e.g., ~1×10^{-3} Scm^{-1} at 500 °C for $Na_{0.5}K_{0.01}Bi_{0.48}Ti_{0.99}Ga_{0.01}O_{2.97}$).[101] Recent studies have demonstrated that the water content of the starting materials affects the stoichiometry of the final products. When reagents are dried, the initial stoichiometry is altered slightly, but the bulk conductivity and conduction mechanisms are significantly altered.[100] NBT-based materials require additional research to overcome issues, such as preparation difficulty and instability in low pO_2 environments.

1.7 Layered perovskites

Layered perovskites have layered structures consist of ABO_3 perovskite or ABO_3 perovskite-like layers. Layered perovskite-type oxides such as double perovskite,[104,105,106,107,108,109] BIMEVOX,[110,111,112] Aurivillius phase,[49,113,114] Ruddlesden-Popper phase,[14,15,115,116,117,118,119,120] brownmillerite,[121,122] and hexagonal perovskite derivative,[123,124,125,126,25] $BaNdInO_4$-based oxides[127,128,129,130] exhibit high oxide-ion conductivities.

Brownmillerite $Ba_2In_2O_5$ is an oxide-ion conductor with layered perovskite structure. The general formula for brownmillerite is $A_2B_2O_5$. It has octahedral BO_6 layers, tetrahedral $BO4$ layers, and *A* cations in its crystal structure. Oxide-ion conductivities of ~10^{-1} Scm^{-1} at 950 °C (high-temperature cubic phase) and ~10^{-3} Scm^{-1} at 800 °C have been reported for $Ba_2In_2O_5$ (low-temperature orthorhombic phase).[121,122] At 925 °C, the orthorhombic-to-cubic phase transition leads to a jump in ionic conductivity by more than an order of magnitude.[121] The order-disorder transition of oxygen vacancies between layers of octahedrally coordinated indium atoms is demonstrated by NMR and thermal analysis at 925 °C. The high oxide-ion conductivities are due to the mobility of oxygen vacancies in the cubic phase between crystallographically equivalent oxygen sites. The high-temperature cubic phase can be stabilized at lower temperatures by substituting Ce, Ti, Ga, and Si for In cation and Sr and La for Ba cation.[131,132,133] However, these $Ba_2In_2O_5$-based substances are typically unstable in CO_2 and reducing environments.[121,134] Matsumoto et al. examined the migration of oxide ions in brownmillerite-type Ca_2AlMnO_5 (reduced phase) and $Ca_2AlMnO_{5.5}$ (oxidized phase) using the nudged elastic band method.[135] They hypothesized that oxide ions diffuse in a two-dimensional manner in $Ca_2AlMnO_{5.5}$ and a one-dimensional manner in Ca_2AlMnO_5. Through an interstitialcy mechanism, oxide ions migrate within AlO_6 layers in the [100] and [001] directions in $Ca_2AlMnO_{5.5}$ (**Fig. 7**).[135] Many brownmillerite-type compounds exhibit proton conduction, including $Sr_2Co_2O_5$ and $Ba_2In_{1.85}M_{0.15}O_6H_2$ (*M* = In, Ga, Sc, and Y).[136,137]

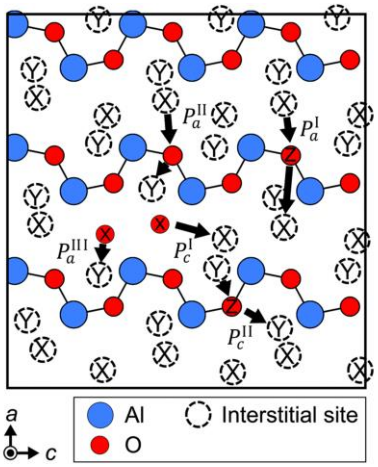

Fig. 7 Elementary paths for oxygen diffusion in Ca_2AlMnO_5 within an AlO_4 layer. Symbols *X* and *Y* represent two symmetrically unique interstitial sites, and *Z* represents an O3 site. Black arrows indicate the direction of oxygen migration. Copyright ©2022 The Royal Society of Chemistry.[135]

Ruddlesden-Popper (R-P) phases are layered perovskites with the formula $A_{n+1}B_nO_{3n+1}$ (*n*: natural number). For *n* = 1, the R-P phase A_2BO_4 has the structure of K_2NiF_4. The structure consists of *n* perovskite ABO_3 slabs interspersed with rock-salt *AO* layers, thereby forming a framework in which *n* layers of BO_6 octahedra are stacked and separated by the *AO* interlayers.[138] Doped $Sr_3Ti_2O_7$ compounds are the first examples of oxide-ion conductors within the R-P family (oxide-ion conductivity of ~10^{-4} Scm^{-1} at about 900 °C).[139] $Sr_3Ti_2O_7$ crystallizes in the tetragonal space group *I*4/*mmm*, and its structure is composed of perovskite $SrTiO_3$ and rock-salt SrO intergrowths. The doped compounds, in which Ti and Sr have been replaced by various elements, exhibit high ionic conductivities (~10^{-3} Scm^{-1} at 900 °C).[139,140,141,142]

Recently, oxide-ion conductivity in $BaNdInO_4$-based ($NdBaInO_4$-based) compounds has been reported.[127,128,143,144] The crystal structure of $BaNdInO_4$ is composed of alternate stackings of *A*-O (Nd-O) units and perovskite-like $Ba_{6/8}Nd_{2/8}InO_3$ units with an edge-facing mode between the slabs. At 858 °C in air, the ionic conductivity of $BaNdInO_4$ is 3.6×10^{-5} Scm^{-1} with an

activation energy of 0.91(4) eV. Substitutions of Sr and Ca atoms for Nd atoms result in $BaNd_{1-x}M_xInO_{4-x/2}$ (*M* = Ca, Sr) solid solutions and the ability to create oxygen vacancies, which increases the oxide-ion conductivities (e.g., 7.7×10^{-4} Scm^{-1} at 858 °C for $BaNd_{0.9}Sr_{0.1}InO_{3.95}$).[128,129] The oxide conductivity of Ti-doped compound $BaNdIn_{0.8}Ti_{0.2}O_4$ (e.g., around $\log(\sigma/Scm^{-1})$ = -2.5 at 900 °C) is higher than that of the parent compound (e.g., $\log(\sigma/Scm^{-1})$ = -4.5 at 858 °C). It is hypothesized that interstitial oxygen atoms in the rock-salt layer are responsible for the higher ionic conductivities in Ti-doped compounds.[145] However, additional investigation is required for the following reasons: (i) Diffraction analyses provide no direct evidence for the interstitial oxygen. (ii) There is no rock-salt layer in the $BaNdInO_4$-type structure, but there is a rare earth oxide unit.[146] Recent reports also mention proton conduction in the doped $BaNdInO_4$ and $BaNdScO_4$ compounds.[143,147]

BIMEVOX materials are a category of oxide-ion conductors based on $Bi_4V_2O_{11}$, the parent compound (BIVOX).[110,114] These materials have a structure of the Aurivillius type, which consists of a perovskite slab $(A_{n-1}BnO3_{n+1})^{2-}$ and a bismuth oxide layer $(Bi_2O_2)^{2+}$. $Bi_4V_2O_{11}$ demonstrates (i) the monoclinic α-orthorhombic β phase transition at 447 °C and (ii) the β-tetragonal γ phase transition at 567 °C. The γ phase has higher ionic conductivities than the α and β phases (~0.20 Scm^{-1} at 670 °C).[110] In the γ phase, oxygen atoms (O1) form the basis of bismuth oxide layers and serve as the skeleton of the whole structure, whereas oxygen atoms (O2 and O3) around vanadium form perovskite-like $VO_{3.5}$ slabs at 16*n* split positions. The vanadium environment is characterized by tetrahedra, octahedra, and trigonal bipyramidal polyhedra superimposed upon one another. The high ionic conductivity of the γ phase is a result of the occupation and positional disorder of O2 and O3 oxygen atoms in $VO_{3.5}$ slabs. Molecular dynamics simulations suggested that the oxide ions in BIVOX primarily migrate in the <110> direction in the vanadium layers.[148] However, due to their instability in reducing environments, the usefulness of BIMEVOX materials is limited.[111,149] In reality, both Bi^{3+} and V^{5+} can be reduced in reducing atmospheres, resulting in an increase in electronic conductivity, formation of metallic bismuth, Bi_2O_3, and $V_{0.9}Bi_{8.1}O_{14}$ phases.[111,112,150] By adding La to the BIMEVOX materials, the good stability of the γ phase is achieved, but the performance is much worse compared to the stabilised zirconia when used as an electrolyte in fuel cells.[149]

1.8 Hexagonal perovskite derivatives

Perovskite-type and related structures can be divided into four structural groups: (i) AMX_3 perovskite-type, (ii) AMX_3-related, (iii) hexagonal perovskite-related, and (iv) modular structures, where *A, M*, and *X* are larger and smaller cations and anions, respectively.[93] The hexagonal perovskite-related structures have hexagonal close packing of AX_3 layers or sequences of hexagonal (h) and cubic (c) AX_3 (and/or anion-deficient AX_{3-x} (c′) where *x* is the number of anion vacancies in an AX_{3-x} layer) layers.

In 2016, Fop et al., reported the hexavalent perovskite derivative $Ba_3MoNbO_{8.5}$.[124] At a temperature of 600 °C, the bulk ionic conductivity σ_b reaches a maximum of 2.2×10^{-3} Scm^{-1}. The oxide-ion transport number demonstrated that $Ba_3MoNbO_{8.5}$ is an ideal oxide-ion conductor. The structure of $Ba_3MoNbO_{8.5}$ is a hybrid of the 9R polytype and the palmierite structure, with a disordered distribution of $(Mo/Nb)O_6$ octahedra and $(Mo/Nb)O_4$ tetrahedra in the c' layer. Oxide ions migrate in two dimensions via mixed O2 octahedral and O3 tetrahedral oxygen sites along the O2–O2–O2 face of the $(Mo/Nb)O_5$ polyhedron (**Fig. 8**).[125] Yashima et al., asserted that the oxide-ion O2–O3 migration and O_2/O_3 disorders in the mixed tetrahedral and octahedral geometry are accountable for the high oxide-ion conductivity.[125] In addition, $Ba_3MoNbO_{8.5}$ is stable over a broad range of pO_2 values. The high ionic conductivities and good stability in wide pO_2 ranges of $Ba_3MoNbO_{8.5}$ suggest that the hexagonal perovskite-related oxides provide a new design approach for oxide-ion conductors. Other hexagonal perovskite derivatives, such as $Ba_3NbWO_{8.5}$,[ref.151] $Ba_3VWO_{8.5}$,[ref.152,153] $Ba_3Nb_{1-x}V_xMoO_{8.5}$,[ref.154] $Ba_3WNbO_{8.5}$,[ref.155] $Ba_3W_{1.2}Nb_{0.8}O_{8.6}$[ref.156] are also oxide-ion conductors.

ARTICLE

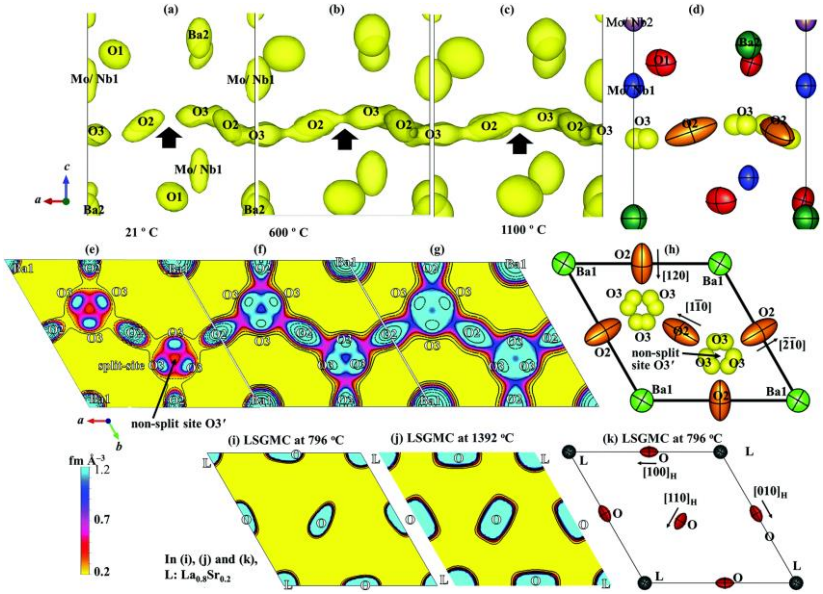

Fig. 8 Experimental visualization of oxide-ion diffusion pathways and occupational and positional disorders through MEM neutron-scattering length density (NSLD) analysis using *in situ* neutron-diffraction data of $Ba_3MoNbO_{8.5-\delta}$ taken at 21, 600, and 1100 °C. (a–c) Yellow isosurfaces of the NSLD at 1.0 fm Å^{-3} of $Ba_3MoNbO_{8.5-\delta}$ at (a) 21, (b) 600 and (c) 1100 °C ($0 \le x, y \le 1$, $0.2 \le z \le 0.5$). (e–g) NSLD distributions on the (001) plane of $Ba_3MoNbO_{8.5-\delta}$ at (e) 21, (f) 600, and (g) 1100 °C. (d and h) Refined crystal structure of $Ba_3MoNbO_{8.5-\delta}$ (= $Ba_3MoNbO_{8.34}$, $\delta = 0.16(3)$) at 1100 °C, viewed along the (d) *b* and (h) *c* axes. The arrow in (a–c) indicates the bottleneck for the O2–O3 migration where the NSLD has a minimum value at each temperature. Contour lines (e–g, i and j) from 0.2 to 1.2 fm Å^{-3}, step 0.1 fm Å^{-3}. Thermal ellipsoids in panels (d, h and k) are drawn at the 50% probability level. In panels (h and k), the directions of anisotropic thermal motions are indicated by arrows, and $[hkl]_H$ in (k) denotes the direction index of the hexagonal lattice.

The hexagonal perovskite derivative $Ba_7Nb_4MoO_{20}$ has a bulk ion conductivity (oxide-ion + proton) of 4.0 mScm^{-1} at 510 °C in a humid atmosphere. $Ba_7Nb_4MoO_{20}$ is a novel candidate for applications as electrolytes in SOFCs, PCFCs, and other energy technologies due to its combination of oxide-ion and proton conduction, as well as its excellent chemical and electrical stability.[126] The crystal structure of $Ba_7Nb_4MoO_{20}$ has the stacking of hexagonal close-packed BaO_3 layers, cubic close-packed BaO_3 layers, and intrinsically oxygen-deficient cubic close-packed c′ layers (h, c and c′, respectively) with sequence (c′hhcchh). The Mo^{6+} and Nb^{5+} cations are assumed to be disordered, and a small portion of the Nb/Mo cations occupy the 2*d* site (1/3, 2/3, ≈0.19), with an occupancy factor ranging from ≈0.05 to 0.13.[ref.126] The structure's intrinsic lack of oxygen contributes to the rapid conduction of oxide ions. Oxide ions migrate predominantly in the c' layers, along a 2D diffusional pathway composed of tetrahedral and octahedral oxygens.[126,157,158]

Substituting the Nb^{5+} cation in $Ba_7Nb_4MoO_{20}$ with an aliovalent cation, such as Mo^{6+}, W^{6+}, and Cr^{6+} can increase its oxide-ion conductivity.[25,157,158,159] $Ba_7Nb_{3.9}Mo_{1.1}O_{20.05}$,[ref.25] $Ba_7Nb_{3.85}W_{0.15}MoO_{20.075}$,[ref.157] $Ba_7Nb_{3.8}Cr_{0.2}MoO_{20.1-\delta}$,[ref.158] and $Ba_7Ta_{3.7}Mo_{1.3}O_{20.15}$,[ref.159] have greater conductivities than $Ba_7Nb_4MoO_{20}$. Particularly, the bulk oxide-ion conductivity of $Ba_7Nb_{3.9}Mo_{1.1}O_{20.05}$ is as high as 5.8×10^{-4} Scm^{-1} at 310 °C, with a low oxide-ion conductivity activation energy. The interstitial oxygen site, O5, exists in the oxygen-deficient layer and is essential for the high oxide-ion conductivity. Oxide ions diffuse through the interstitial O5 and lattice O1 sites, resulting in a 2D interstitialcy diffusion through the O1—O5 pathway (

Fig. 9).[25] The similarity between the diffusion paths of $Ba_7Nb_{3.9}Mo_{1.1}O_{20.05}$ and $Ba_3MoNbO_{8.5-\delta}$ suggests that the oxide-ion diffusion pathway on the oxygen-deficient layer is a characteristic shared by hexagonal perovskite-related oxides. This characteristic would guide the design of oxide-ion conductors with perovskite-related hexagonal structures.

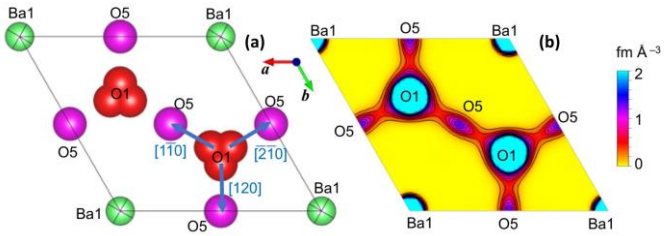

Fig. 9 Refined crystal structure (a) and corresponding MEM NSLD distribution (b) on the *ab* plane at $z = 0$ of $Ba_7Nb_{3.9}Mo_{1.1}O_{20.05}$ at 800 °C. In (b), the contour lines from 0 to 2 fm Å^{-3} by the step of 0.2 fm Å^{-3}. Arrows in (a) denote the directions of oxide-ion O1-to-O5 migration.

2. Oxide-ion conduction in Dion–Jacobson phases

2.1 Introduction of Dion–Jacobson phases

The Dion–Jacobson phases have layered perovskite structures and a general formula of $A'[A_{n-1}B_nO_{3n+1}]$ (A' = H, Cs, Rb, Li, Ag; A = Ca, Sr, Bi, rare earths such as La, metal halide complexes such as CuBr and FeCl; B = transition metals such as Ti, Nb, Ta; n indicates the number of the BO_6 octahedral layers [$n > 2$]).[160,161] The oxide ions in $A'[A_{n-1}B_nO_{3n+1}]$ can be partially substituted by fluorine and nitrogen anions. The crystal structures of Dion–Jacobson layered perovskites consist of the stacking of perovskite and/or perovskite-like $[A_{n-1}B_nO_{3n+1}]$ slab and A' layer (**Fig. 10**). These structures can be regarded as stacking of perovskite and/or perovskite-like $[A_{n-1}B_nO_{3n+1}]$ slab and CsCl-type $[A'O]$ layers (**Fig. 10**).

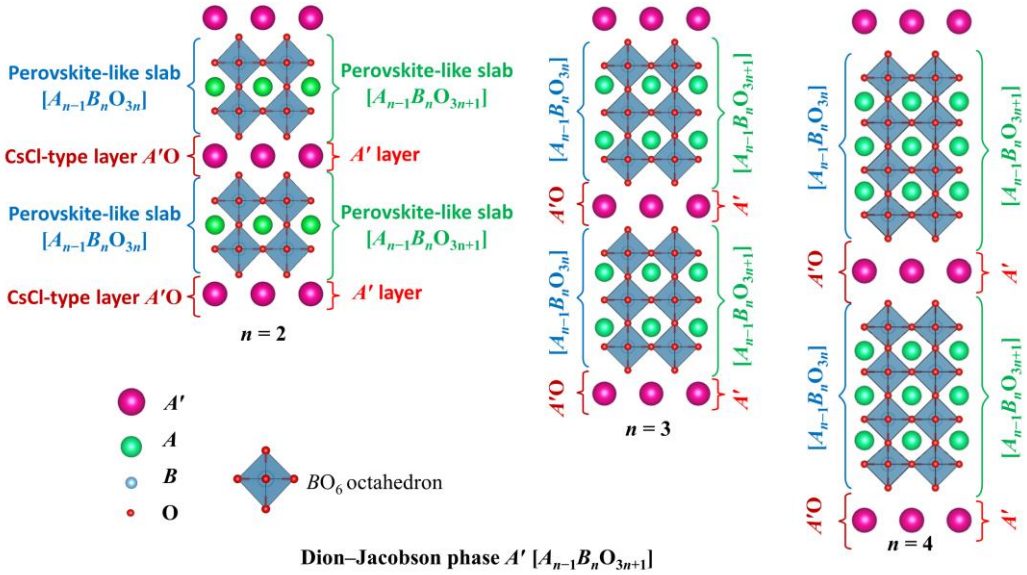

Fig. 10 Crystal structures of typical examples of Dion–Jacobson layered perovskites $A'[A_{n-1}B_nO_{3n+1}]$, where n=2, n=3, and n=4. Blue square denotes a BO_6 octahedron.

Although the material properties of Dion–Jacobson-type layered perovskites have not been studied as extensively as ABO_3 perovskites and their related compounds, there have been reports on ferroelectricity,[162] proton conduction,[163,164] lithium-ion conduction,[165,166] sodium-ion conduction,[161,166] and mixed proton-electron conduction[167] in the Dion-Jacobson-type layered perovskites.

The ferroelectric properties of orthorhombic Dion–Jacobson-type layered perovskites $CsBiNb_2O_7$ and $RbBiNb_2O_7$ were examined.[168] Subramanian et al.,[168] was the first to report these compounds. The interlayer alkali ions of cesium (Cs^+) and rubidium (Rb^+) are easily exchanged by protons (H^+), which enables proton conduction of ~10^{-6} Scm^{-1} at 100–300 °C with activation energies of 0.68–0.72 eV. Leakage and proton conduction of $CsBiNb_2O_7$ were reported by Goff et al.[169]

Lithium ionic conduction in Dion–Jacobson-type layered perovskites $LiLaTa_2O_7$ and $LiLaTa_2O_{6.15}N_{0.57}$ were examined by Kim et al.[165] The ionic conductivities of $LiLaTa_2O_7$ and $LiLaTa_2O_{6.15}N_{0.57}$ are higher than that of the similar Ruddlesden-Popper phase $Li_2La_{2/3}Ta_2O_7$. In the Dion–Jacobson phases $LiLaTa_2O_7$ and $LiLaTa_2O_{6.15}N_{0.57}$, only half of the lithium sites are occupied, which encourages lithium ion hopping. In contrast, the Ruddlesden-Popper phase $Li_2La_{2/3}Ta_2O_7$ has only fully occupied lithium sites, thereby restricting lithium ion migration. As far as alkali ion conduction (interlayer ion conduction) is concerned, the Dion–Jacobson phases might be more promising than the Ruddlesden-Popper phases.

Sodium-ion conduction was confirmed in the Dion–Jacobson-type layered perovskite $NaCa_2Nb_3O_{10}$ by AC impedance spectroscopy and dc Hebb-Wagner polarization measurements.[170] The electrical conductivities are almost independent of the pO_2 in the range from 0.21 to 10^{-6} atm. The open-circuit voltage measurements revealed no oxide-ion conduction in $NaCa_2Nb_3O_{10}$. The transport number of Na^+ ions at 550 °C is 0.95 and varies with temperature and atmosphere.[170]

Oxide-ion conduction in perovskite and perovskite-related materials has been extensively studied. Our group has published only three papers on oxide-ion conduction in Dion–Jacobson layered perovskites between 2020 and 2022.[171,172,173] This article focuses on the recent advancements of Dion–Jacobson-type layered oxide-ion conductors, with a particular emphasis on $CsM_2Ti_2NbO_{10-\delta}$ (M = Bi and lanthanoids; δ represents the number of oxygen vacancies). In this article, we also discuss the structural characteristics of $CsM_2Ti_2NbO_{110-\delta}$ materials.

Our group reported oxide-ion conduction in Dion–Jacobson perovskites in $CsBi_2Ti_2NbO_{10-\delta}$ in 2020.[171] Using available crystallographic data and the bond-valence method, we screened Dion–Jacobson phases and chose $CsBi_2Ti_2NbO_{10-\delta}$

because the bond-valence-based energy barrier for oxide-ion migration is relatively low (E_b = 0.5 eV; **Fig. 11**).[171]

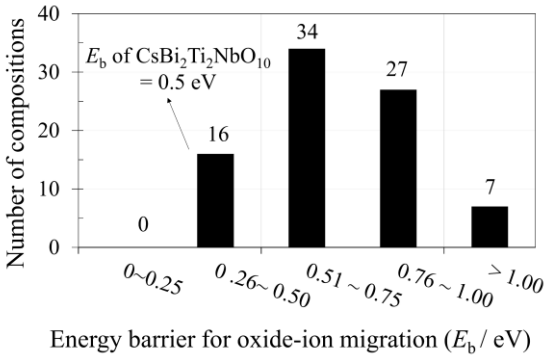

Fig. 11 Histogram of the bond-valence-based energy barriers E_b for the oxide-ion migration of the 69 Dion-Jacobson phases using 83 crystallographic data. Copyright © 2020 Springer Nature.[171]

2.2 Crystal structures of $CsBi_2Ti_2NbO_{10-\delta}$ and $CsLa_2Ti_2NbO_{10-\delta}$

$CsBi_2Ti_2NbO_{10-\delta}$ has an orthorhombic structure (**Fig, 12a** and **Fig. 13a**) at low temperatures (24–540 °C) and a tetragonal structure (**Fig. 13b**) at high temperatures (560–800 °C). The tilting of octahedra and displacement of bismuth ions produce the orthorhombic phase with low symmetry. Rietveld refinements of synchrotron X-ray and neutron diffraction data measured in air and vacuum, respectively, confirmed the phase transition.[171] On heating, Rietveld refinements were conducted with a single *Ima*2 structure at 24–540 °C and a single *P*4/*mmm* structure at 560–800 °C (**Fig. 12a, b**). The phase transition exhibits a hysteresis of approximately 20 °C, indicating that $CsBi_2Ti_2NbO_{10-\delta}$ undergoes a first-order phase transition. In general, the first-order phase transition degrades conductivity, device stability, and durability in oxide-ion conductors like Bi_2O_3,[8] $La_2Mo_2O_9$,[78] $Bi_4V_2O_{11}$,[110] and $Ba_2In_2O_5$[121]. In contrast to $CsBi_2Ti_2NbO_{10-\delta}$, $CsLa_2Ti_2NbO_{10-\delta}$ was reported to be a single tetragonal phase with a space group of *P*4/*mmm* from 24 °C to 800 °C (**Fig. 13c**) [172,174], exhibiting no first-order phase transitions. Further examination on the detailed crystal structure of $CsLa_2Ti_2NbO_{10-\delta}$ is needed in the future, because reflections forbidden for the primitive tetragonal symmetry are observed.[174]

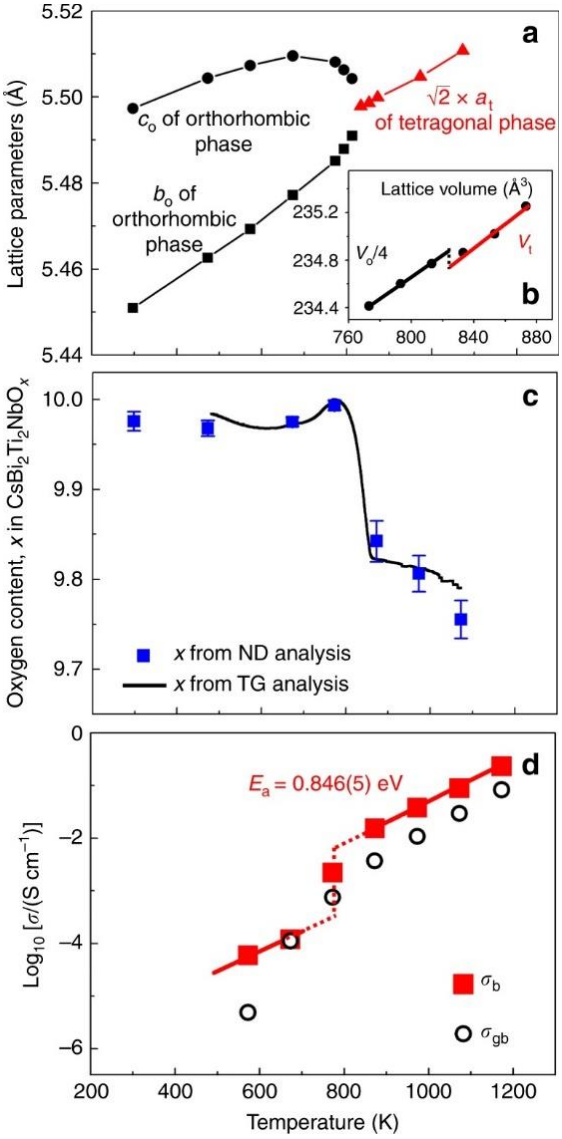

Fig. 12 Temperature dependences of lattice parameters, oxygen content, and conductivities. Lattice parameters (a) and reduced lattice volume (b) of $CsBi_2Ti_2NbO_{10-\delta}$, which were refined using synchrotron X-ray powder diffraction data measured *in situ* at high temperatures in static air on heating. Subscripts o and t denote orthorhombic and tetragonal, respectively. (c) Oxygen contents of $CsBi_2Ti_2NbO_{10-\delta}$ on heating, which were obtained by thermogravimetric (TG) analysis in dry air (black line) and calculated from occupancy factors refined using *in situ* neutron-diffraction (ND) data in vacuum (blue marks). (d) Bulk electrical conductivity σ_b and grain boundary conductivity σ_{gb} of $CsBi_2Ti_2NbO_{10-\delta}$ in dry air on heating. Copyright © 2020 Springer Nature.[171]

ARTICLE

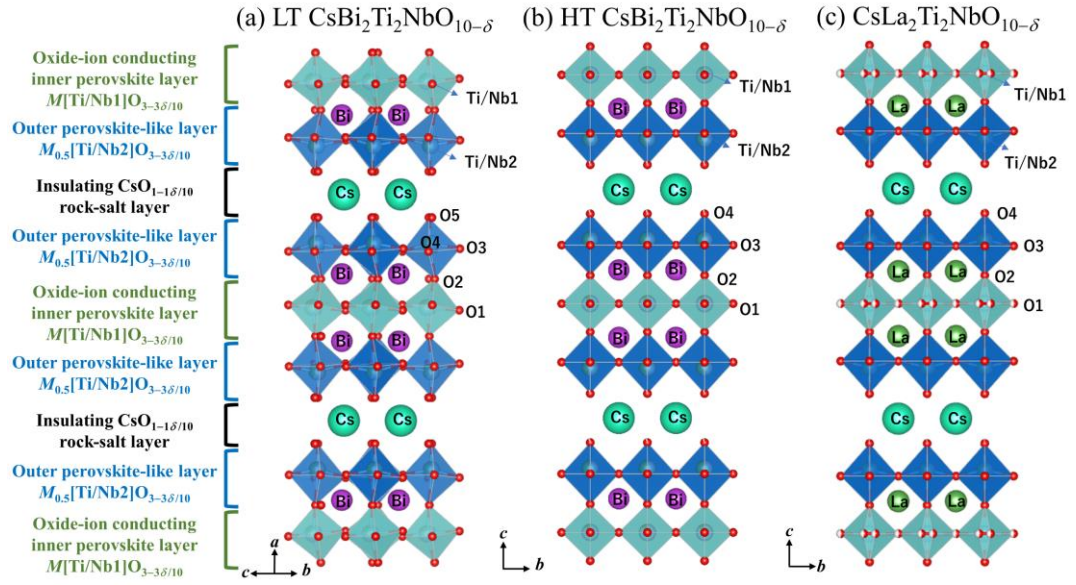

Fig. 13 Refined crystal structures of orthorhombic $CsBi_2Ti_2NbO_{10-\delta}$ at low-temperature (LT), tetragonal $CsBi_2Ti_2NbO_{10-\delta}$ at high-temperature (HT) tetragonal $CsLa_2Ti_2NbO_{10-\delta}$ refined using neutron-diffraction data. The green and blue squares denote the $(Ti/Nb1)O_{6-6\delta/10}$ and $(Ti/Nb2)O_{6-6\delta/10}$ octahedra, respectively. The Ti/Nb1 site in the inner perovskite layers is nearly fully occupied by Ti cations and Ti/Nb2 site is statistically occupied by Ti and Nb cations in the outer perovskite layers. Copyright © 2020 Springer Nature.[171]

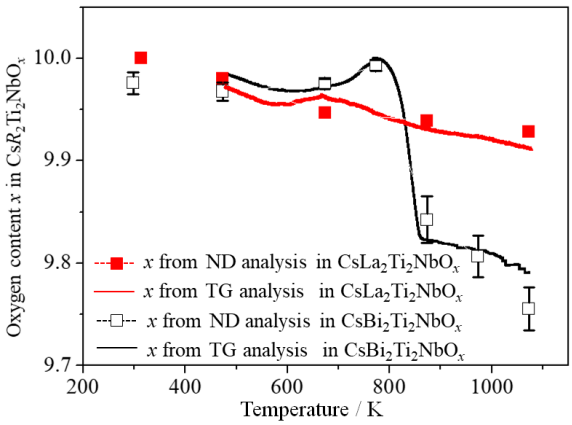

Fig. 14 Oxygen contents of $CsBi_2Ti_2NbO_{10-\delta}$ and $CsLa_2Ti_2NbO_{10-\delta}$, which are obtained by thermogravimetric (TG) analysis in dry air) and calculated from occupancy factors refined using in situ neutron-diffraction (ND) data in vacuum.

$CsM_2Ti_2NbO_{10-\delta}$ oxides (M = Bi and La) have a layered perovskite structure with an inner perovskite layer $M[Ti/Nb_1]O_{3-3\delta/10}$, two perovskite-like layers $M_{0.5}[Ti/Nb2]O_{3-3\delta/10}$, and a $CsO_{3-3\delta/10}$ rock-salt layer (**Fig. 13**).[171,172] Ti/Nb1 and Ti/Nb2 represent two distinct B sites in $CsM_2Ti_2NbO_{10-\delta}$ (= $CsM_2B_3O_{10-\delta}$). According to DFT calculations, the Ti/Nb_1 site is nearly completely occupied by Ti cations, whereas the Ti/Nb_2 site is statistically occupied by Ti and Nb cations.[171,172] Electrostatic forces contribute to the occupation of Ti^{4+} and Nb^{5+} cations by the negatively charged $CsO_{1-\delta/10}$ layer.[172,175] The estimated bond-valence sums for the refined crystal structures of $CsM_2Ti_2NbO_{10-\delta}$ (M = Bi and La) are close to their formal charges, validating the refined crystal structures. Significant oxygen vacancies exist in $CsM_2Ti_2NbO_{10}$ at temperatures above 600 °C, as confirmed by the oxygen occupancy factors refined using variable temperature neutron-diffraction data and the oxygen contents estimated by the thermogravimetric analysis (**Figs. 12c** and **14**).

2.3 Oxide-ion conduction of $CsBi_2Ti_2NbO_{10-\delta}$, $CsLa_2Ti_2NbO_{10-\delta}$, and their solid solutions

The bulk conductivity σ_b of $CsBi_2Ti_2NbO_{10-\delta}$ is 2.7×10^{-4} Scm^{-1} at 450 °C and 3.4×10^{-3} Scm^{-1} at 500 °C (**Fig. 15d**). The abruptly increased σ_b of $CsBi_2Ti_2NbO_{10-\delta}$ around 500 °C is ascribed to the increase in oxygen vacancy concentration (**Fig. 12c**) and the orthorhombic-to-tetragonal phase transition (**Figs. 12a** and **12b**). $CsLa_2Ti_2NbO_{10-\delta}$ has a lower σ_b (e.g., 4.1×10^{-4} Scm^{-1} at 900 °C) than $CsBi_2Ti_2NbO_{10-\delta}$ (8.9×10^{-2} Scm^{-1} at 900 °C), (**Fig. 16d**). The σ_b of $CsBi_2Ti_2NbO_{10-\delta}$ in the high temperature range of 500–900 °C is higher than that of YSZ and comparable to that of well-known oxide-ion conductors (**Fig. 17**). An oxygen concentration cell measured the oxide-ion transport numbers of $CsBi_2Ti_2NbO_{10-\delta}$ to be >0.98 at 600–900 °C in air/O_2, >0.95 at

600–900 °C in air/N_2, and 0.87 at 600 °C in air/5% H_2 in N_2 (**Fig. 15a**). In contrast, the oxide-ion transport number of $CsLa_2Ti_2NbO_{10-\delta}$ decreases with temperature increase from 0.99 at 600 °C to 0.42 at 1000 °C under air/N_2 conditions (Fig. 16a). At 600 °C, the results indicated that the predominant carrier in $CsLa_2Ti_2NbO_{10-\delta}$ is oxide ion. The total DC conductivity (σ_{DC}) is nearly independent of pO_2 over wide pO_2 regions in $CsM_2Ti_2NbO_{10-\delta}$ (**Figs. 15b** and **16b**; e.g., from 10^{-22} to 1 atm for $CsLa_2Ti_2NbO_{10-\delta}$ at 600 °C and from 10^{-22} to 1 atm for $CsBi_2Ti_2NbO_{10-\delta}$ at 700 °C), indicating the dominance of oxide. In the low pO_2 region of $CsM_2Ti_2NbO_{10-\delta}$, the conductivities increase indicating n-type electronic conduction (**Figs. 15b** and **16b**). In a reducing atmosphere, the reduction of Ti^{4+} and Nb^{5+} cations may lead to the formation of oxygen vacancies and electronic defects. In a reducing atmosphere, n-type electronic conduction is typically observed in oxide-ion conductors containing Ti and Nb. There is no proton conduction at 600–900 °C for $CsBi_2Ti_2NbO_{10-\delta}$ and 400–1000 °C for $CsLa_2Ti_2NbO_{10-\delta}$, as the total conductivities measured in dry air are nearly identical to those measured in moist air (**Figs. 15c** and **16c**).

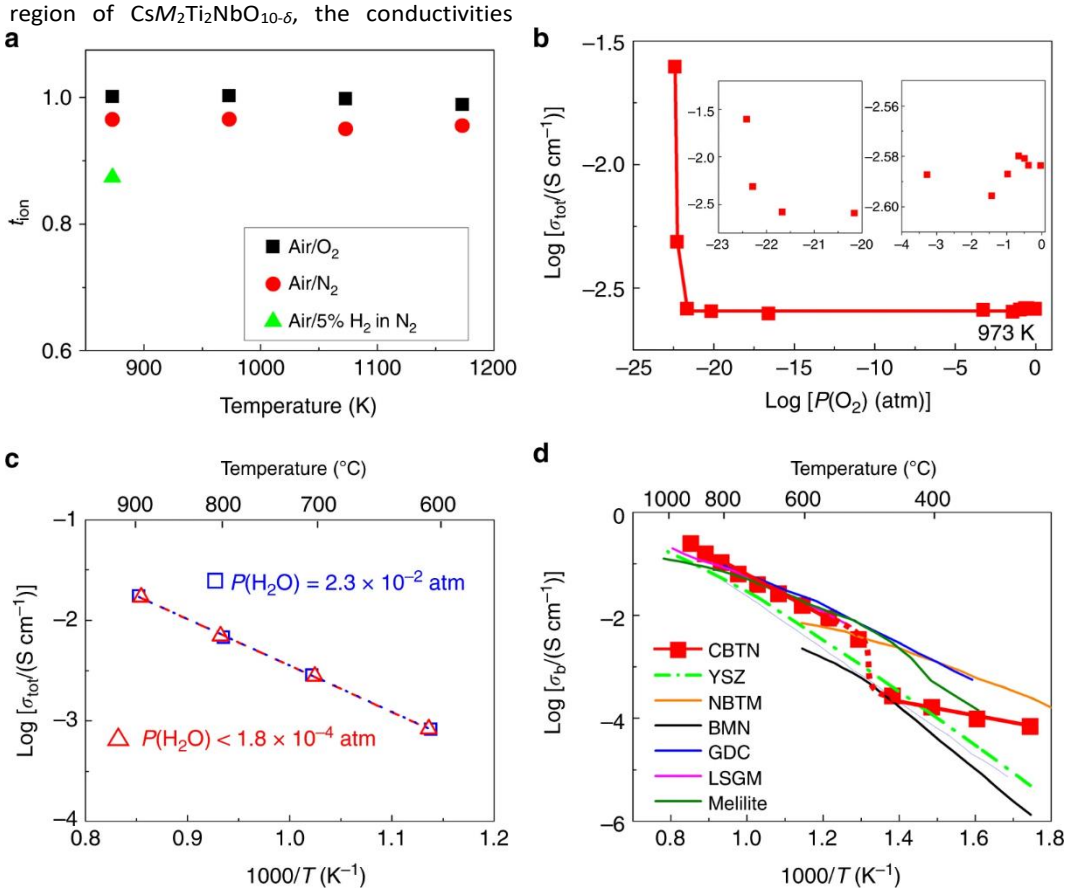

Fig. 15 Oxide-ion conduction of $CsBi_2Ti_2NbO_{10-\delta}$. (a) Oxide-ion transport number t_{ion} determined by oxygen concentration cell measurements of $CsBi_2Ti_2NbO_{10-\delta}$. (b) Partial oxygen pressure $P(O_2)$ dependence of total DC electrical conductivities σ_{tot} of $CsBi_2Ti_2NbO_{10-\delta}$ at 973 K and the insets show the zoom-in view of high and low $P(O_2)$ regions. (c) Arrhenius plots of σ_{tot} of $CsBi_2Ti_2NbO_{10-\delta}$ in dry and wet air. (d) Comparison of bulk conductivity σ_b of $CsBi_2Ti_2NbO_{10-\delta}$ (CBTN) on cooling with those of best oxide-ion conductors: $(Y_2O_3)_{0.08}(ZrO_2)_{0.92}$ (YSZ)[176], $Na_{0.5}Bi_{0.49}Ti_{0.98}Mg_{0.02}O_{2.965}$ (NBTM)[88], $Ba_3MoNbO_{8.5}$ (BMN)[124], $Ce_{0.9}Gd_{0.1}O_{1.95}$ (GDC)[177], $La_{0.9}Sr_{0.1}Ga_{0.8}Mg_{0.2}O_{2.85}$ (LSGM)[87], and $La_{1.54}Sr_{0.46}Ga_3O_{7.27}$ (melilite)[17]. Copyright © 2020 Springer Nature.[171]

ARTICLE

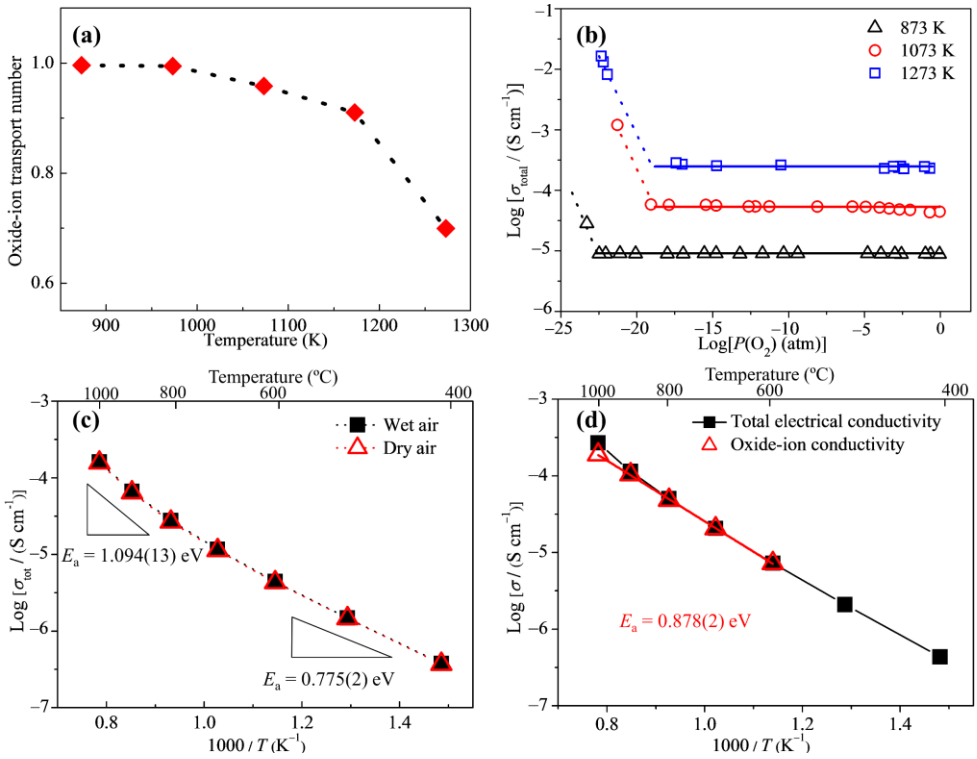

Fig. 16 (a) Oxide-ion transport number of $CsLa_2Ti_2NbO_{10-\delta}$ in air/(O_2 and N_2 gas mixture); (b) partial oxygen pressure $P(O_2)$ dependence of the total electrical conductivities σ_{tot} of $CsLa_2Ti_2NbO_{10-\delta}$ at 873 K, 1073 K, and 1273 K; (c) Arrhenius plots of σ_{tot} of $CsLa_2Ti_2NbO_{10-\delta}$ under dry and wet flowing air conditions; and (d) Arrhenius plots of the σ_b of $CsLa_2Ti_2NbO_{10-\delta}$ and $CsBi_2Ti_2NbO_{10-\delta}$ on cooling. Copyright © 2020 The Royal Society of Chemistry.[172]

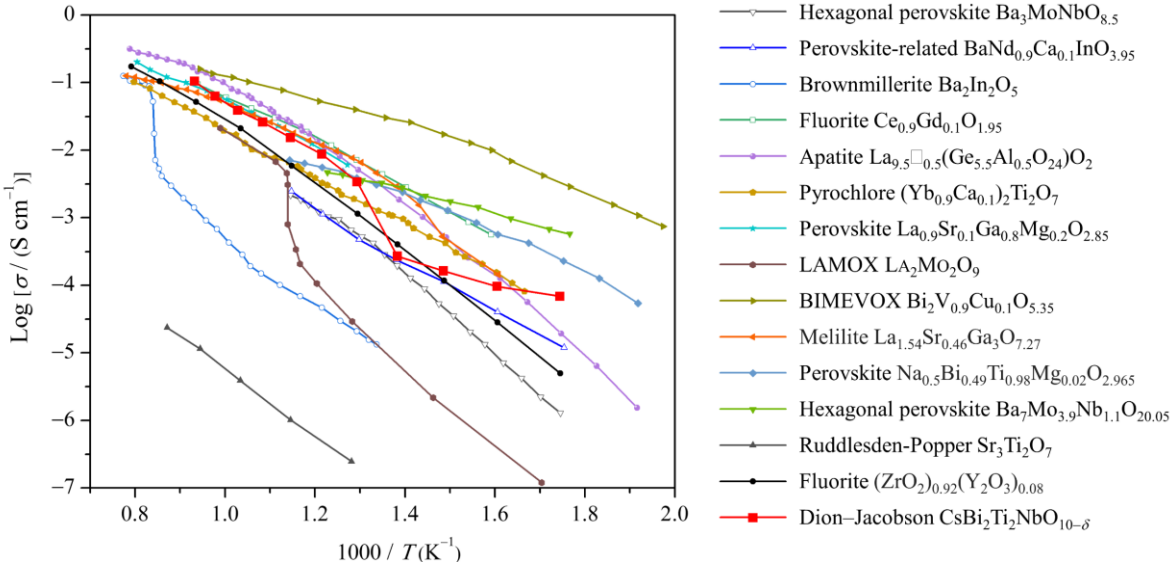

Fig. 17 Comparison of bulk conductivity σ_b of $CsBi_2Ti_2NbO_{10-\delta}$ (CBTN)[171] with those of best oxide-ion conductors: hexagonal perovskite $Ba_3MoNbO_{8.5}$ (ref.[88]), perovskite-related $BaNd_{0.9}Ca_{0.1}InO_{3.95}$ (ref.[129]), brownmillerite $Ba_2In_2O_5$ (ref.[121]), fluorite $Ce_{0.9}Gd_{0.1}O_{1.95}$ (ref.[177]), apatite $La_{9.5}\square_{0.5}(Ge_{5.5}Al_{0.5}O_{24})O_2$ (ref.[178]), pyrochlore $(Yb_{0.9}Ca_{0.1})_2Ti_2O_7$ (ref.[179]), perovskite $La_{0.9}Sr_{0.1}Ga_{0.8}Mg_{0.2}O_{2.85}$ (ref. [87]), LAMOX $La_2Mo_2O_9$ (ref.[78]), BIMEVOX $Bi_2V_{0.9}Cu_{0.1}O_{5.35}$ (ref.[180]), melilite $La_{1.54}Sr_{0.46}Ga_3O_{7.27}$ (ref.[17]), perovskite $Na_{0.5}Bi_{0.49}Ti_{0.98}Mg_{0.02}O_{2.965}$ (ref.[88]), hexagonal perovskite $Ba_7Mo_{3.9}Nb_{1.1}O_{20.05}$ (ref.[25]), Ruddlesden-Popper $Sr_3Ti_2O_7$ (ref.[141]), and fluorite $(ZrO_2)_{0.92}(Y_2O_3)_{0.08}$ (ref.[176]).

ARTICLE

The activation energy of $CsLa_2Ti_2NbO_{10-\delta}$ is greater than that of $CsBi_2Ti_2NbO_{10-\delta}$. The bottlenecks are the Bi–Bi–Ti triangles for $CsBi_2Ti_2NbO_{10-\delta}$ and La–La–Ti triangles for $CsLa_2Ti_2NbO_{10-\delta}$, respectively. At 800 °C, the La^{3+} cation has a smaller ionic radius than the Bi^{3+} cation, resulting in smaller oxide-ion migration bottlenecks [0.9924(2) Å for $CsLa_2Ti_2NbO_{10-\delta}$ and 1.0229(6) Å for $CsBi_2Ti_2NbO_{10-\delta}$ at 800 °C. The smaller bottleneck is attributable to the higher activation energy of $CsLa_2Ti_2NbO_{10-\delta}$. Electrical measurements demonstrate the high phase stability of $CsBi_2Ti_2NbO_{10-\delta}$ and $CsLa_2Ti_2NbO_{10-\delta}$ at high temperatures and varying pO_2 values. There is no significant difference between the results obtained before and after the electrical measurements.

Through aliovalent substitution or doping, the oxide-ion conductivities of many materials can be enhanced, resulting in the formation of oxygen defects (oxygen vacancies and/or interstitial oxygen) and/or a lower activation energy. We therefore synthesized the *A*-site substituted materials $CsBi_{2-x}M_xTi_2NbO_{10-x/2}$ (*M* = Mg, Ca, Sr, and Ba, *x* = 0.1, 0.2) and the *B*-site substituted oxides $CsBi_2Ti_{2-x}Nb_{1+x}O_{10+x/2}$ (*x* = 0.1, 0.2, -0.1 and -0.2), and measured their total DC conductivities. For *A*-site substituted compounds, the substitution of Bi^{3+} with Sr^{2+} enhances the conductivity of the mother phase $CsBi_2Ti_2NbO_{10-\delta}$ (**Fig. 18**).[173] At temperatures between 600 and 900 °C, the total DC conductivities of all solid solutions of $CsBi_2Ti_{2-x}Nb_{1+x}O_{10+x/2}$ (*x* = 0.1, 0.2, -0.1, and -0.2) are greater than those of the parent phase (**Fig. 19**). The successful enhancement of conductivity through substitutions would advance the science and technology of Dion–Jacobson-type oxide-ion conductors.

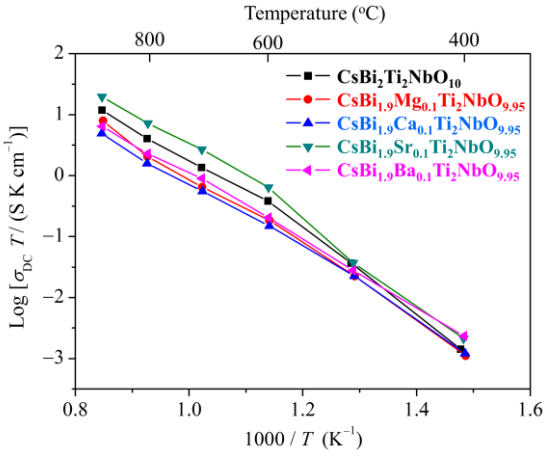

Fig. 18 Arrhenius plots of the total DC conductivity (σ_{DC}) for $CsBi_{1.9}M_{0.1}Ti_2NbO_{9.95}$ (*M* = Mg, Ca, Sr and Ba) and mother material $CsBi_2Ti_2NbO_{10}$ in air.

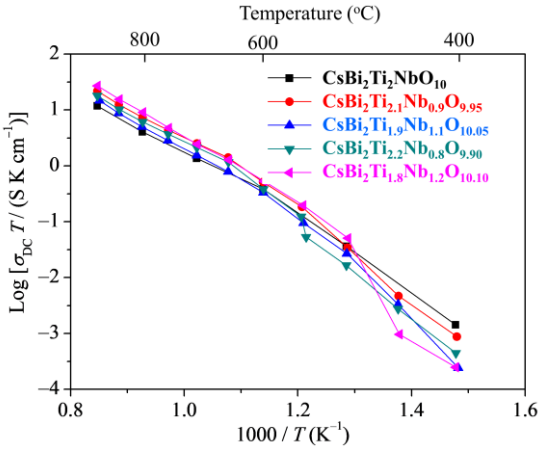

Fig. 19 Arrhenius plots of the total DC conductivity (σ_{DC}) for $CsBi_2Ti_{2-x}Nb_{1+x}O_{10+x/2}$ (*x* = 0.1, 0.2, -0.1 and -0.2) and mother material $CsBi_2Ti_2NbO_{10}$ in air.

2.4 Structure-conductivity relationships of $CsBi_2Ti_2NbO_{10-\delta}$ and $CsLa_2Ti_2NbO_{10-\delta}$

Oxide-ion conductivity is related to oxygen defects and crystalline structures. Similar structural origins underlie oxide-ion conduction in $CsBi_2Ti_2NbO_{10-\delta}$ and $CsLa_2Ti_2NbO_{10-\delta}$. Using the refined structure of high-temperature tetragonal $CsBi_2Ti_2NbO_{9.80(2)}$ at 700 °C, this paper discusses the structure-conductivity correlation (**Fig. 20a**).

ARTICLE

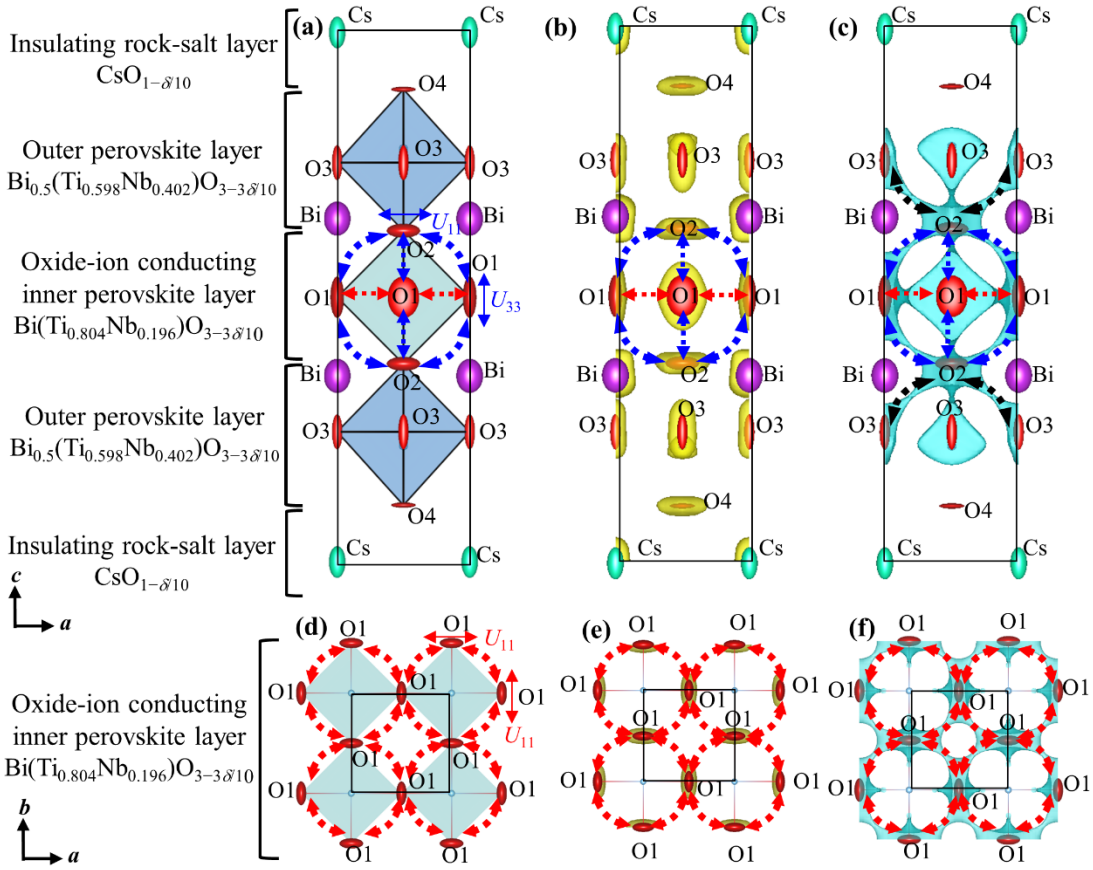

Fig. 20 (a), (d) Refined crystal structure of $CsBi_2Ti_2NbO_{9.80(2)}$ at 973 K, which is obtained through Rietveld analysis of in situ neutron-diffraction data. (b), (e) Yellow isosurfaces of the neutron scattering length density at 1.0 fm Å^{-3} with the structure (973 K). (c), (f) Blue isosurfaces of the bond-valence-based energy for an oxide ion at 0.6 eV for the structure at 973 K. Blue, red, and black dotted lines with arrows denote the possible O1-O2, O1-O1, and O2-O3 diffusion pathways of oxide ion, respectively. The solid lines with arrows in a and d stand for the directions of anisotropic thermal motions of O1 and O2 oxygen atoms. Thermal ellipsoids are drawn at the 50% probability level. Regions of (a)–(c) $-1/2 \le x, y, z \le 1/2$ and of (d)–(f) $-1/2 \le x, y \le 3/2$, $0 \le z \le 0.1$. Copyright © 2020 Springer Nature.[171]

To obtain the accurate information of oxygen atoms, the high-temperature neutron-diffraction data of $CsBi_2Ti_2NbO_{10}$ were measured using the super-high-resolution diffractometer SuperHRPD.[181,182,183] In the crystal structure of tetragonal $CsBi_2Ti_2NbO_{10-\delta}$ (**Fig. 20a**), there are four oxygen sites: (1) equatorial oxygen O1 site in the inner perovskite $Bi(Ti_{0.8}0_4Nb_{0.196})O_{3-3\delta/10}$ layer, (2) apical oxygen O2 site in the inner perovskite $Bi(Ti_{0.8}0_4Nb_{0.196})O_{3-3\delta/10}$ layer, (3) equatorial oxygen O3 site in the outer perovskite $Bi_{0.5}(Ti_{0.598}Nb_{0.402})O_{3-3\delta/10}$ layer, and (4) apical oxygen O4 site in the outer perovskite $Bi_{0.5}(Ti_{0.598}Nb_{0.402})O_{3-3\delta/10}$ layer (**Figs. 13** and **20**). The refined equivalent isotropic atomic displacement parameters (ADPs) of O1 and O2 atoms are significantly greater than those of O3 and O4 atoms, indicating that the O1 and O2 atoms exhibit greater thermal motions than O3 and O4 atoms. The values of anisotropic ADPs (U_{ij}) of oxygen atoms (e.g., U_{11} = 0.0901(19) Å^2, U_{33} = 0.157(3) Å^2 >> U_{22} = 0.0170(14) Å^2 for O1 and $U_{11} = U_{22}$ = 0.1010(11) Å^2 >> U_{33} = 0.0181(17) Å^2 for O2) indicate anisotropic thermal motions in the structure along different axes. The extremely large anisotropic ADPs U_{ij} of the O1 (U_{11} and U_{33}) and O2 atoms (U_{11} and U_{22}) suggest the O1–O2 (blue dotted arrows in **Fig. 20**) and O1–O1 bonds (the red-dotted arrows in **Fig. 20**) oxide-ion diffusion.

Neutron scattering length density (NSLD) was analyzed utilizing the maximum-entropy technique (MEM).[12,13,14,54,184,185] The isosurfaces of NSLD (yellow isosurfaces in **Figs. 20b** and **20e**) exhibit anisotropic thermal motions of O1 and O2 atoms, providing support for oxide-ion O1–O1 and O1–O2 migrations. In addition, the bond-valence-based energy landscapes support O1–O1 and O1–O2 oxide-ion diffusion (BVELs, blue isosurfaces in **Figs. 20c** and **20f**). The BVELs also suggest an additional O2–O3 diffusion route.

As a conclusion, oxide ions diffuse along the edges of the $Bi(Ti_{0.804}Nb_{0.196})O_{3-3\delta/10}$ octahedra in the inner perovskite layer in a two-dimensional manner. Therefore, the inner perovskite layer is referred to as "oxide-ion conducting inner perovskite layer $Bi(Ti_{0.804}Nb_{0.196})O_{3-3\delta/10}$". The high oxide-ion conductivities of $CsBi_2Ti_2NbO_{10-\delta}$ are due to the presence of oxygen vacancies, the 2D oxide-ion conducting inner perovskite layers, and the large anisotropic thermal motions of the oxygen atoms.

$CsLa_2Ti_2NbO_{10-\delta}$ has a lower oxide-ion conductivity than $CsBi_2Ti_2NbO_{10-\delta}$ due to its smaller oxygen atom ADPs, smaller oxide-ion migration bottlenecks, and lower oxygen-vacancy concentration of $CsLa_2Ti_2NbO_{10-\delta}$ (**Fig. 14**). For instance, the equivalent isotropic ADPs of O1 at 800 °C in $CsLa_2Ti_2NbO_{10-\delta}$ is 0.0275(6) Å^2, whereas in $CsBi_2Ti_2NbO_{10-\delta}$ it is 0.0849(5) Å^2. At 800 °C, the oxygen vacancy δ in $CsBi_2Ti_2NbO_{10-\delta}$ is 0.084(6), which is less than the oxygen vacancy in $CsBi_2Ti_2NbO_{10-\delta}$, which is 0.278(4). Doping and/or modification are anticipated to increase the oxygen-vacancy concentration in$CsBi_2Ti_2NbO_{10-\delta}$.[128,129,154] High oxide-ion conductivity in $CsBi_2Ti_2NbO_{10-\delta}$ can also be attributed to the Bi^{3+} species, which has been reported to play an important role in oxide-ion conduction in numerous Bi-containing materials.[45,88]

New oxide-ion conductors necessitate a deeper comprehension of the structural origin of oxide-ion diffusion. In cubic ABO_3 perovskites, such as $La_{0.9}Sr_{0.1}Ga_{0.9}Mg_{0.1}O_{2.9}$, oxide ions migrate along a curved path through the edges of the BO_6 octahedra.[91,97,186,187,188] Cubic ABO_3 perovskites exhibit 3D oxide-ion diffusion and low activation energies between 0.5 and 0.9 eV.[187]

Conversely, double perovskite oxide-ion conductors with a cation-ordered layered structure $AA'B_2O_{5+\delta}$display anisotropic and two-dimensional oxide-ion diffusion. Oxide ions in double perovskite $PrBaCo_2O_{5+\delta}$, for instance, diffuse through equatorial oxygen (O3) and deficient apical oxygen (O2) sites along the edges of the $CoO_{4.734}$ octahedra in the Pr-(defective O2) and adjacent Co-O3 planes, demonstrating 2D and highly anisotropic oxide-ion diffusion (**Figs. 21a** and **21b**). To explain the highly 2D anisotropic oxide-ion diffusion, a concept was presented. Due to the fact that the radius of Ba^{2+} is greater than that of Pr^{3+}, the coordination number of oxygen atoms surrounding Ba atoms increases, while it decreases around Pr atoms. Consequently, a higher oxygen vacancy concentration was obtained around the Pr atoms at the O2 site, leading to the O2-O3-O2 highway of mobile oxide ions in the Pr-Co-O slabs (called oxide-ion conducting layers).[107]

3. Concepts in the design of oxide-ion conductors

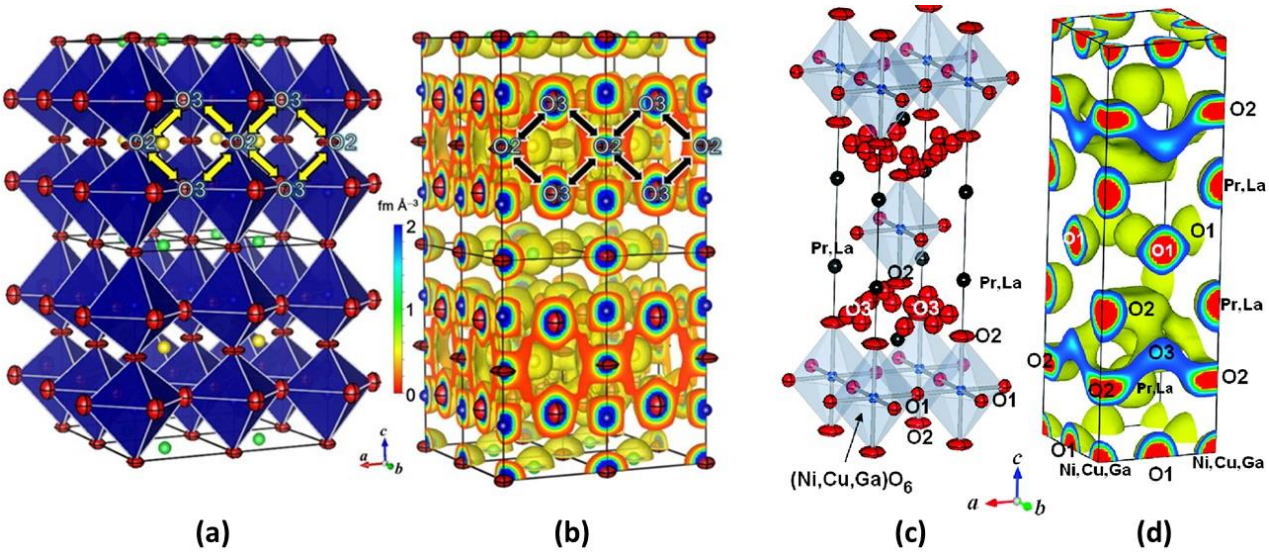

Fig. 21 (a) Refined crystal structure of $PrBaCo_2O_{5.357}$ at 1000 °C drawn with blue CoO_6 octahedra and red oxygen thermal ellipsoids. Yellow and green spheres denote Pr and Ba atoms, respectively. (b) Nuclear-density distributions on the *bc* and *ca* planes and yellow isosurface of nuclear density at 0.085 fm Å^{-3} of $PrBaCo_2O_{5.357}$ at 1000 °C. (c) Refined crystal structure and (d) isosurface of nuclear density at 0.05 fm Å^{-3} of the mixed oxide-ion and electronic conductor $(Pr_{0.9}La_{0.1})_2(Ni_{0.74}Cu_{0.21}Ga_{0.05})O_{4+\delta}$ determined in situ at 1015.6 °C. Copyright © 2013 American Chemical Society for (a) and (b) [107] and copyright © 2008 American Chemical Society for (c) and (d).[15]

The K_2NiF_4-type structure of the Ruddlesden-Popper layered perovskite $(Pr_{0.9}La_{0.1})_2(Ni_{0.74}Cu_{0.21}Ga_{0.05})O_{4+\delta}$ (PLNCG) consists of a $(Pr_{0.9}La_{0.1})(Ni_{0.74}Cu_{0.21}Ga_{0.05})O_3$ perovskite and a $(Pr_{0.9}La_{0.1})O$ rock-salt layer. The migration of mobile oxide ions through oxygen vacancies in solids, such as the above-discussed cubic perovskite and double perovskite oxide-in conductors, is typically responsible for the migration of oxide ions. However, the oxide-ion diffusion mechanism in the PLNCG hops via interstitial oxide ions, as explained by the following novel concept. Using diffraction experiments and theoretical calculations, the interstitial oxygen atoms O3 around (0.6, 0, 0.2) in the $(Pr_{0.9}La_{0.1})O$ rock-salt layers are identified (**Fig. 21c**). O2 atoms at the apex exhibit a significant anisotropic thermal

motion. Oxide ions diffuse through anisotropic O2 and interstitial O3 sites in PLNCG, thereby forming a 2D network of oxygen diffusion pathways. Interstitial O3 is indispensable for the high oxide-ion diffusion of PLNCG (**Fig. 21d**).[15] Producing more interstitial oxide ions in the O3 sites, such as by doping the Ga^{3+} cation at the Ni^{2+} site, can increase the oxide-ion conductivity in K_2NiF_4-type structures, according to the interstitialcy diffusion mechanism.[14,189]

As stated previously, a comprehensive understanding of the relationship between crystal structure and oxide-ion conduction will be helpful when designing new oxide-ion conductors. As previously described, the oxide-ion diffusion mechanism in Dion–Jacobson phases has been clarified. Oxide ions diffuse two-dimensionally through oxygen vacancies in the oxide-ion conducting inner perovskite layers via the O1-O2 and O1-O1 oxide-ion diffusion pathways. The Dion–Jacobson phase structure must be better understood to explain why the inner perovskite layer is an oxide-ion conducting layer via the O1-O2 and O1–O1 oxide-ion diffusion pathways.

We proposed a theory to explain the high oxide-ion conductivities of layered Dion–Jacobson perovskites.[171] The *A*-*A*-*B* (Bi-Bi-Ti/Nb1 and La-La-Ti/Nb1) triangles in Dion–Jacobson layered perovskites $CsM_2Ti_2NbO_{10-\delta}$ (*M* = Bi, La) are the bottlenecks for oxide-ion migration (the red and green triangles in **Fig. 22**). The large size of *A*' cations (Cs^+) and displacement of *A* cations (Bi^{3+} and La^{3+}) enlarge the bottlenecks of oxide-ion migration within the structure. The new concept can be used to explain the large bottlenecks, as detailed below. Larger *A*' cations expand the *A*–*A* distance along the *b* axis (the green arrows in **Fig. 22**) due to the occupational ordering of the larger *A*' cations and relatively smaller *A* cations. The longer *A*–*A* distance along the *b* axis expands the bottleneck of *A*–*A*–*B* triangles (green triangles in **Fig. 22**). Cations in *A* site are displaced along the *c* axis apart from the inner perovskite layer (the red arrows in **Fig. 22**) by electrostatic forces. The displacement of *A* cations along the *c* axis increases the *A*–*A* distance. The longer *A*–*A* distance along the *c* axis enlarges the bottleneck of *A*–*A*–*B* triangles (red triangles in **Fig. 22**). The increase in *A*–*A* distance axes creates large bottlenecks for oxide-ion diffusion in the inner perovskite layers, causing the layers to become oxide-ion conducting layers and the oxygen atoms in the layers to become mobile oxide ions. In conclusion, we propose a novel idea: large bottlenecks for oxide-ion migration caused by the large size of *A*' cations and the displacement of *A* cations. High oxide-ion conductivities in $CsBi_2Ti_2NbO_{10-\delta}$, $CsLa_2Ti_2NbO_{10-\delta}$, and their solid solutions can be explained using the new concept. Comparing the bottleneck sizes of $CsBi_2Ti_2NbO_{10-\delta}$ to those of other layered perovskites with the same Bi–Bi–Ti triangles, such as, $BaBi_4Ti_4O_{15}$,[190] $Bi_4Ti_3O_{12}$,[191] and $Bi_2Sr_2TiNb_2O_{12}$[192], is one example. The layered perovskite of the Dion–Jacobson type, $CsBi_2Ti_2NbO_{10-\delta}$, has larger Bi–Bi–Ti triangle bottlenecks, lower activation energy, and consequently higher oxide-ion conductivities.

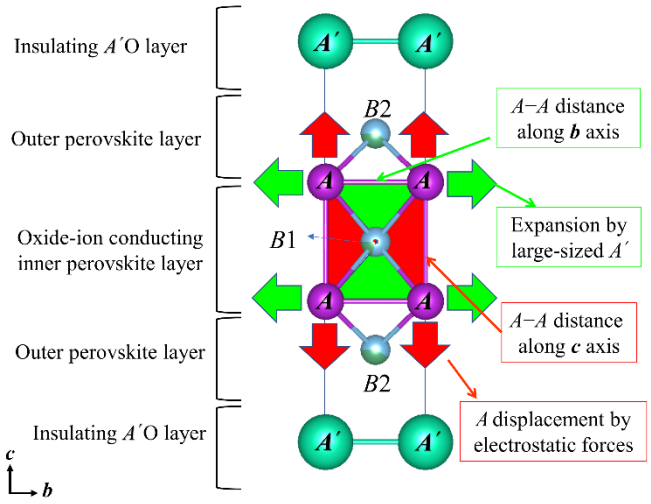

Fig. 22 New concept of enlarged bottlenecks for oxide-ion migration created by the large size of *A*' cations and *A* cation displacement in Dion-Jacobson-type layered perovskite $CsM_2Ti_2NbO_{10-\delta}$. Red and green triangles denote the areas of bottlenecks oxide-ion migration. Oxygen atoms are omitted for simplicity in the structure.

4. Conclusions and outlook

The Dion–Jacobson phase $CsBi_2Ti_2NbO_{10-\delta}$ is a new structural family of oxide-ion conductors with high bulk ionic conductivities (e.g., 8.9×10^{-2} Scm^{-1} at 800 °C) and high phase stability at high temperatures and in wide pO_2 regions. The high oxide-ion conductivities are attributable to the presence of oxygen vacancies, anisotropic and 2D oxide-ion diffusion of the oxygen atoms (O1 ando2) in the inner oxide-ion conducting perovskite layers, and presence of large oxide-ion migration bottlenecks. To explain the high oxide-ion conductivities of Dion–Jacobson-type oxide-ion conductors, a novel concept has been proposed. The discovery and proposed concept of Dion–Jacobson-type oxide ion conductors will facilitate the design of new oxide ion conductors and offer significant growth potential in the energy, environmental, and biomedical sectors. The Dion–Jacobson-type oxide-ion conductors are largely unexplored; consequently, there are numerous issues and studies to be conducted, as outlined below:

(1) Dion–Jacobson-type oxide-ion conductors with high ionic conductivity and no phase transitions are necessary.
(2) The stability of Bi-containing compounds such as $CsBi_2Ti_2NbO_{10-\delta}$ under reducing conditions (H_2 gas) should be investigated and improved.
(3) Substituting of Cs by other alkali cations in $CsM_2Ti_2NbO_{10-\delta}$ should be studied, which will help us to understand the concept more directly by comparing the bottlenecks and the carrier mobility.
(4) Only the ionic conduction of *n* = 3 of $A'[A_{n-1}B_nO_{3n+1}]$ compounds has been investigated, whereas the electrical properties of *n* = 2, 4, and 5 compounds remain unknown.

(5) Electronic conduction of the n-type occurs in a reducing environment, which can be resolved by substitution. For instance, K^+ and Ga^{3+} co-doped $Na_{0.5}Bi_{0.5}TiO_3$ oxide-ion conductor strengthens the stability in a reducing,[101] and by adding La to the BIMEVOX materials, excellent stability has been achieved when using it as the electrolyte in solid oxide fuel cells.[149]
(6) Theoretical calculations, such as ab initio molecular dynamics, need to be carried out to evidence the oxide-ion diffusion mechanism.

Conflicts of interest

There are no conflicts to declare.

Acknowledgements

This study was partly supported by Grants-in-Aid for Scientific Research (KAKENHI, JP20K20293, JP21K20483 and 21K18182) from the Ministry of Education, Culture, Sports, Science and Technology of Japan, Adaptable and Seamless Technology transfer Program through Target-driven R&D (A-STEP) from Japan Science and Technology Agency (JST) Grant Number JPMJTR22TC and JSPS Core-to-Core Program, A. Advanced Research Networks (Solid Oxide Interfaces for Faster Ion Transport; Mixed Anion Research for Energy Conversion [JPJSCCA20200004]), and by a research granted from the Murata Science Foundation and the Tokuyama Science Foundation.

ARTICLE

Notes and references

1 W. C. Heraeus, *Zeitschrift für Elektrotechnik und Elektrochemie*, 1899, **6**, 41–43.
2 Y. Liu, J. Parisi, X. Sun and Y. Lei, *J. Mater. Chem. A*, 2014, **2**, 9919–9943.
3 L. Malavasi, C. A. J. Fisher and M. S. Islam, *Chem. Soc. Rev.*, 2010, **39**, 4370–4387.
4 P. Vernoux, L. Lizarraga, M. N. Tsampas, F. M. Sapountzi, A. De Lucas-Consuegra, J. L. Valverde, S. Souentie, C. G. Vayenas, D. Tsiplakides, S. Balomenou and E. A. Baranova, *Chem. Rev.*, 2013, **113**, 8192–8260.
5 P. N. Dyer, R. E. Richards, S. L. Russek and D. M. Taylor, *Solid State Ionics*, 2000, **134**, 21–33.
6 J. C. Boivin and G. Mairesse, *Chem. Mater.*, 1998, **10**, 2870–2888.
7 J. B. Goodenough, *Nature*, 2000, **404**, 821–823.
8 V. V. Kharton, E. N. Naumovich, A. A. Yaremchenko and F. M. B. Marques, *J. Solid State Electrochem.*, 2001, **5**, 160–187.
9 S. J. Skinner and J. A. Kilner, *Mater. Today*, 2003, **6**, 30–37.
10 B. C. Steele and A. Heinzel, *Nature*, 2001, **414**, 345–352.
11 Z. Shao and S. M. Haile, *Nature*, 2004, **431**, 170–173.
12 M. Yashima, *J. Ceram. Soc. Japan*, 2009, **117**, 1055–1059.
13 M. Yashima, *Catal. Today*, 2015, **253**, 3–19.
14 M. Yashima, N. Sirkanda and T. Ishihara, *J. Am. Chem. Soc.*, 2010, **132**, 2385–2392.
15 M. Yashima, M. Enoki, T. Wakita, R. Ali, Y. Matsushita, F. Izumi and T. Ishihara, *J. Am. Chem. Soc.*, 2008, **130**, 2762–2763.
16 A. Fujimoto, M. Yashima, K. Fujii and J. R. Hester, *J. Phys. Chem. C*, 2017, **121**, 21272–21280.
17 X. Kuang, M. A. Green, H. Niu, P. Zajdel, C. Dickinson, J. B. Claridge, L. Jantsky and M. J. Rosseinsky, *Nat. Mater.*, 2008, **7**, 498–504.
18 J. A. Kilner and R. J. Brook, *Solid State Ionics*, 1982, **6**, 237–252.
19 S. Nakayama and M. Sakamoto, *J. Eur. Ceram. Soc.*, 1998, **18**, 1413–1418.
20 J. A. Kilner, *Solid State Ionics*, 2000, **129**, 13–23.
21 K. Huang, R. S. Tichy and J. B. Goodenough, *J. Am. Ceram. Soc.*, 1998, **75**, 2565.
22 C. A. López, J. C. Pedregosa, D. G. Lamas and J. A. Alonso, *J. Appl. Crystallogr.*, 2014, **47**, 1395–1401.
23 K. Nakamura, K. Fujii, E. Niwa and M. Yashima, *J. Ceram. Soc. Japan*, 2018, **126**, 292–299.
24 R. Inoue, K. Fujii, M. Shiraiwa, E. Niwa and M. Yashima, *Dalt. Trans.*, 2018, **47**, 7515–7521.
25 M. Yashima, T. Tsujiguchi, Y. Sakuda, Y. Yasui, Y. Zhou, K. Fujii, S. Torii, T. Kamiyama and S. J. Skinner, *Nat. Commun.*, 2021, **12**, 556.
26 M. Yashima, *Solid State Ionics*, 2008, **179**, 797–803.
27 Y. Yasui, E. Niwa, M. Matsui, K. Fujii and M. Yashima, *Inorg. Chem.*, 2019, **58**, 9460–9468.
28 E. Niwa and M. Yashima, *ACS Appl. Energy Mater.*, 2018, **1**, 4009–4015.
29 M. Yashima and T. Tsuji, *Chem. Mater.*, 2007, **19**, 3539–3544.
30 M. Coduri, M. Karlsson and L. Malavasi, *J. Mater. Chem. A*, 2022, **10**, 5082–5110.
31 A. Navrotsky, *J. Mater. Chem.*, 2010, **20**, 10577–10587.
32 M. Yashima, S. Kobayashi and T. Yasui, *Solid State Ionics*, 2006, **177**, 211–215.
33 M. Yashima, S. Kobayashi and T. Yasui, *Faraday Discuss.*, 2007, **134**, 369–376.
34 M. Yashima, *J. Phys. Chem. C*, 2009, **113**, 12658–12662.
35 J. H. Lee, M. Yashima and M. Yoshimura, *Solid State Ionics*, 1998, **107**, 47–51.
36 M. Yashima and T. Takizawa, *J. Phys. Chem. C*, 2010, **114**, 2385–2392.
37 M. Yashima, T. Sekikawa, D. Sato, H. Nakano and K. Omoto, *Cryst. Growth Des.*, 2013, **13**, 829–839.
38 Yashima, M., M. Kakihana and M. Yoshimura, *Solid State Ionics*, 1996, **86–88**, 1131–1149.

39 HideakiInaba and HiroakiTagawa, *Solid State Ionics*, 1996, **83**, 1–16.
40 K. Eguchi, T. Setoguchi, T. Inoue and H. Arai, *Solid State Ionics*, 1992, **52**, 165–172.
41 H. A. Harwig and A. G. Gerards, *J. Solid State Chem.*, 1978, **26**, 265–274.
42 M. Yashima and D. Ishimura, *Chem. Phys. Lett.*, 2003, **378**, 395–399.
43 M. Yashima and D. Ishimura, *Appl. Phys. Lett.*, 2005, **87**, 1–3.
44 A. Laarif and F. Theobald, *Solid State Ionics*, 1986, **21**, 183–193.
45 N. M. Sammes, G. A. Tompsett, H. Näfe and F. Aldinger, *J. Eur. Ceram. Soc.*, 1999, **19**, 1801–1826.
46 X. Li, X. Kuang and J. Sun, *Inorg. Chem. Front.*, 2021, **8**, 1374–1398.
47 M. Yashima, D. Ishimura and K. Ohoyama, *J. Am. Ceram. Soc.*, 2005, **88**, 2332–2335.
48 X. Kuang, J. L. Payne, M. R. Johnson and I. E. Radosavljevic, *Angew. Chemie - Int. Ed.*, 2012, **51**, 690–694.
49 J. K. Thomas, M. E. Anderson, W. E. Krause and H. Zur Loye, *MRS Online Proc. Libr. Arch.*, 1993, **293**, 295–300.
50 D. W. Jung, J. C. Nino, K. L. Duncan, S. R. Bishop and E. D. Wachsman, *Ionics (Kiel).*, 2010, **16**, 97–103.
51 M. P. van Dijk, K. J. de Vries and A. J. Burggraaf, *Solid State Ionics*, 1983, **9**–**10**, 913–919.
52 H. L. Tuller, *Solid State Ionics*, 1992, **52**, 135–146.
53 S. A. Kramer and H. L. Tuller, *Solid State Ionics*, 1995, **82**, 15–23.
54 W. Uno, K. Fujii, E. Niwa, S. Torii, P. Miao, T. Kamiyama and M. Yashima, *J. Ceram. Soc. Japan*, 2018, **126**, 341–345.
55 P. J. Wilde and C. R. A. Catlow, *Solid State Ionics*, 1998, **112**, 173–183.
56 M. A. Subramanian, G. Aravamudan and G. V. Subba Rao, *Prog. Solid State Chem.*, 1983, **15**, 55–143.
57 J. Shamblin, M. Feygenson, J. Neuefeind, C. L. Tracy, F. Zhang, S. Finkeldei, D. Bosbach, H. Zhou, R. C. Ewing and M. Lang, *Nat. Mater.*, 2016, **15**, 507–511.
58 L. Zhao, S. Geng, J. Feng, C. Yin and X. Kuang, *J. Solid State Chem.*, 2021, **302**, 122370.
59 F. P. Marlton, Z. Zhang, Y. Zhang, T. E. Proffen, C. D. Ling and B. J. Kennedy, *Chem. Mater.*, 2021, **33**, 1407–1415.
60 C. Tealdi, P. Mustarelli and M. S. Islam, *Adv. Funct. Mater.*, 2010, **20**, 3874–3880.
61 L. Zhou, J. Xu, M. Allix and X. Kuang, *Chem. Rec.*, 2020, **20**, 1117–1128.
62 J. Schuett, T. K. Schultze and S. Grieshammer, *Chem. Mater.*, 2020, **32**, 4442–4450.
63 W. Zhang, J. Feng, F. Lu, A. J. Fernández-Carrión, H. Fu and X. Kuang, *J. Mater. Chem. A*, 2021, **9**, 22064–22071.
64 J. Xu, J. Wang, A. Rakhmatullin, S. Ory, A. J. Fernández-Carrión, H. Yi, X. Kuang and M. Allix, *ACS Appl. Energy Mater.*, 2019, **2**, 2878–2888.
65 K. Fujii, M. Yashima, K. Hibino, M. Shiraiwa, K. Fukuda, S. Nakayama, N. Ishizawa, T. Hanashima and T. Ohhara, *J. Mater. Chem. A*, 2018, **6**, 10835–10846.
66 E. Kendrick, M. S. Islam and P. R. Slater, *J. Mater. Chem.*, 2007, **17**, 3104–3111.
67 T. Wei, J. Xu and W. Zhu, *Energy Sci. Eng.*, 2022, **10**, 525–537.
68 P. R. Slater, J. E. H. Sansom and J. R. Tolchard, *Chem. Rec.*, 2004, **4**, 373–384.
69 S. Tao and J. T. S. Irvine, *Mater. Res. Bull.*, 2001, **36**, 1245–1258.
70 R. Ali, M. Yashima, Y. Matsushita, H. Yoshioka, K. Ohoyama and F. Izumi, *Chem. Mater.*, 2008, **20**, 5203–5208.
71 R. Ali, M. Yashima, Y. Matsushita, H. Yoshioka and F. Izumi, *J. Solid State Chem.*, 2009, **182**, 2846–2851.
72 L. León-Reina, E. R. Losilla, M. Martínez-Lara, S. Bruque and M. A. G. Aranda, *J. Mater. Chem.*, 2004, **14**, 1142–1149.
73 S. Ide, H. Takahashi, I. Yashima, K. Suematsu, K. Watanabe and K. Shimanoe, *J. Phys. Chem. C*, 2020, **124**, 2879–2885.
74 J. R. Peet, M. S. Chambers, A. Piovano, M. R. Johnson and I. R. Evans, *J. Mater. Chem. A*, 2018, **6**, 5129–5135.
75 T. Mina-ai and H. Iwahara, 1992, **52**, 319–325.
76 T. Esaka, R. Tachibana and S. Takai, *Solid State Ionics*, 1996, **92**, 129–133.
77 X. Yang, A. J. Fernández-Carrión, J. Wang, F. Porcher, F. Fayon, M. Allix and X. Kuang, *Nat.*

Commun., , DOI:10.1038/s41467-018-06911-w.
78 Y. Lacorre, P., Goutenoire, F., Bohnke, O., Retoux, R., & Laligant, *Nature*, 2000, **404**, 856–858.
79 F. Goutenoire, O. Isnard, E. Suard, O. Bohnke, Y. Laligant, R. Retoux and P. Lacorre, *J. Mater. Chem.*, 2001, **11**, 119–124.
80 R. Pandey, S. Singh and P. Singh, *J. Mater. Sci. Mater. Electron.*, 2020, **31**, 11325–11335.
81 H. Zhu, P. Zhang and S. Dai, *ACS Catal.*, 2015, **5**, 6370–6385.
82 T. Murakami, J. R. Hester and M. Yashima, *J. Am. Chem. Soc.*, 2020, **142**, 11653–11657.
83 Y. Su, Y. Tsujimoto, K. Fujii, Y. Masubuchi, H. Ohata, H. Iwai, M. Yashima and K. Yamaura, *Chem. Commun.*, 2019, **55**, 7239–7242.
84 W. Zhang, M. Shiraiwa, N. Wang, T. Ma, K. Fujii, E. Niwa and M. Yashima, *J. Ceram. Soc. Japan*, 2018, **126**, 814–819.
85 M. Yashima and R. Ali, *Solid State Ionics*, 2009, **180**, 120–126.
86 R. Ali and M. Yashima, *J. Solid State Chem.*, 2005, **178**, 2867–2872.
87 T. Ishihara, H. Matsuda and Y. Takita, *J. Am. Chem. Soc.*, 1994, **116**, 3801–3803.
88 M. Li, M. J. Pietrowski, R. A. De Souza, H. Zhang, I. M. Reaney, S. N. Cook, J. A. Kilner and D. C. Sinclair, *Nat. Mater.*, 2014, **13**, 31–35.
89 M. S. Islam, *J. Mater. Chem.*, 2000, **10**, 1027–1038.
90 C. Lan, H. Li and S. Zhao, *J. Comput. Electron.*, 2020, **19**, 905–909.
91 Y. C. Chen, M. Yashima, T. Ohta, K. Ohoyama and S. Yamamoto, *J. Phys. Chem. C*, 2012, **116**, 5246–5254.
92 K. Saito, K. Fujii and M. Yashima, *J. Solid State Chem.*, 2022, **306**, 122733.
93 Tilley R. J. D., *Perovskites: Structure-property relationships*, Wiley, Chichester, UK, 2016.
94 T. Ishihara, J. A. Kilner, M. Honda and Y. Takita, *J. Am. Chem. Soc.*, 1997, **119**, 2747–2748.
95 T. Ishihara, H. Matsuda and Y. Takita, *J. Am. Chem. Soc.*, 1994, **116**, 3801–3803.
96 M. Kajitani, M. Matsuda, A. Hoshikawa, K. I. Oikawa, S. Torii, T. Kamiyama, F. Izumi and M. Miyake, *Chem. Mater.*, 2003, **15**, 3468–3473.
97 M. Yashima, K. Nomura, H. Kageyama, Y. Miyazaki, N. Chitose and K. Adachi, *Chem. Phys. Lett.*, 2003, **380**, 391–396.
98 Y. Zhao, J. Kilner, T. Ishihara, K. Yoshizawa and A. Staykov, *J. Phys. Chem. Solids*, , DOI:10.1016/j.jpcs.2021.110393.
99 K. N. Kim, B. K. Kim, J. W. Son, J. Kim, H. W. Lee, J. H. Lee and J. Moon, *Solid State Ionics*, 2006, **177**, 2155–2158.
100 M. Li, H. Zhang, S. N. Cook, L. Li, J. A. Kilner, I. M. Reaney and D. C. Sinclair, *Chem. Mater.*, 2015, **27**, 629–634.
101 X. Xu, X. Liu, R. Rao, Y. Zhao, H. Du and J. Shi, *Ceram. Int.*, 2020, **46**, 22321–22329.
102 J. Huang, F. Zhu, D. Huang, B. Wang, T. Xu, X. Li, P. Fan, F. Xia, J. Xiao and H. Zhang, *Ceram. Int.*, 2016, **42**, 16798–16803.
103 B. Santhoshkumar, K. R. Priolkar, S. Pollastri, D. Oliveira De Souza, I. Carlomagno, A. K. Bera, S. M. Yusuf and B. Pahari, *J. Phys. Chem. C*, , DOI:10.1021/acs.jpcc.1c04995.
104 S. Sengodan, S. Choi, A. Jun, T. H. Shin, Y.-W. Ju, H. Y. Jeong, J. Shin, J. T. S. Irvine and G. Kim, *Nat. Mater.*, 2014, **14**, 205–209.
105 R. Ali, M. Yashima and F. Izumi, *Chem. Mater.*, 2007, **19**, 3260–3264.
106 M. Burriel, J. Peña-Martínez, R. J. Chater, S. Fearn, A. V. Berenov, S. J. Skinner and J. a. Kilner, *Chem. Mater.*, 2012, **24**, 613–621.
107 Y. C. Chen, M. Yashima, J. Peña-Martínez and J. A. Kilner, *Chem. Mater.*, 2013, **25**, 2638–2641.
108 W. Zhang, Z. Zhang, L. Gao and T. Ma, *Prog. Chem.*, 2016, **28**, 961–974.
109 F. Hesse, I. Da Silva and J. W. G. Bos, *Chem. Mater.*, 2022, **34**, 1191–1202.
110 F. Abraham, J. C. Boivin, G. Mairesse and G. Nowogrocki, *Solid State Ionics*, 1990, **40**–**41**, 934–937.
111 T. Iharada, A. Hammouche, J. Fouletier, M. Kleitz, J. C. Boivin and G. Mairesse, *Solid State Ionics*, 1991, **48**, 257–265.
112 C. Pirovano, M. C. Steil, E. Capoen, G. Nowogrocki and R. N. Vannier, *Solid State Ionics*, 2005, **176**, 2079–2083.
113 K. R. Kendall, C. Navas, J. K. Thomas and H. C. Zur Loye, *Chem. Mater.*, 1996, **8**, 642–649.
114 D. G. Porob and T. N. Guru Row, *Chem. Mater.*, 2000, **12**, 3658–3661.

115 G. Amow and S. J. Skinner, *J. Solid State Electrochem.*, 2006, **10**, 538–546.
116 M. V. Patrakeev, I. A. Leonidov, V. L. Kozhevnikov and V. V. Kharton, *Solid State Sci.*, 2004, **6**, 907–913.
117 A. Yamada, Y. Suzuki, K. Saka, M. Uehara, D. Mori, R. Kanno, T. Kiguchi, F. Mauvy and J.-C. Grenier, *Adv. Mater.*, 2008, **20**, 4124–4128.
118 G. Yang, C. Su, R. Ran, M. O. Tade and Z. Shao, *Energy and Fuels*, 2014, **28**, 356–362.
119 H. Yaguchi, K. Fujii, Y. Tsuchiya, H. Ogino, Y. Tsujimoto and M. Yashima, *ACS Appl. Energy Mater.*, 2022, **5**, 295–304.
120 Y. Wang, K. Yamamoto, Y. Tsujimoto, T. Matsunaga, D. Zhang, Z. Cao, K. Nakanishi, T. Uchiyama, T. Watanabe, T. Takami, H. Miki, H. Iba, K. Maeda, H. Kageyama and Y. Uchimoto, *Chem. Mater.*, 2022, **34**, 609–616.
121 J. B. Goodenough, J. E. Ruiz-Diaz and Y. S. Zhen, *Solid State Ionics*, 1990, **44**, 21–31.
122 J. E. Auckett, A. J. Studer, E. Pellegrini, J. Ollivier, M. R. Johnson, H. Schober, W. Miiller and C. D. Ling, *Chem. Mater.*, 2013, **25**, 3080–3087.
123 S. Fop, K. S. McCombie, E. J. Wildman, J. M. S. Skakle and A. C. Mclaughlin, *Chem. Commun.*, 2019, **55**, 2127–2137.
124 S. Fop, J. M. S. Skakle, A. C. McLaughlin, P. A. Connor, J. T. S. Irvine, R. I. Smith and E. J. Wildman, *J. Am. Chem. Soc.*, 2016, **138**, 16764–16769.
125 M. Yashima, T. Tsujiguchi, K. Fujii, E. Niwa, S. Nishioka, J. R. Hester and K. Maeda, *J. Mater. Chem. A*, 2019, **7**, 13910–13916.
126 S. Fop, K. S. McCombie, E. J. Wildman, J. M. S. Skakle, J. T. S. Irvine, P. A. Connor, C. Savaniu, C. Ritter and A. C. Mclaughlin, *Nat. Mater.*, 2020, **19**, 752–757.
127 K. Fujii, Y. Esaki, K. Omoto, M. Yashima, A. Hoshikawa, T. Ishigaki and J. R. Hester, *Chem. Mater.*, 2014, **26**, 2488–2491.
128 K. Fujii, M. Shiraiwa, Y. Esaki, M. Yashima, S. J. Kim and S. Lee, *J. Mater. Chem. A*, 2015, **3**, 11985–11990.
129 X. Yang, S. Liu, F. Lu, J. Xu and X. Kuang, *J. Phys. Chem. C*, 2016, **120**, 6416–6426.
130 M. Shiraiwa, K. Fujii, Y. Esaki, S. J. Kim, S. Lee and M. Yashima, *J. Electrochem. Soc.*, 2017, **164**, F1392–F1399.
131 T. Yao, Y. Uchimoto, M. Kinuhata, T. Inagaki and H. Yoshida, *Solid State Ionics*, 2000, **132**, 189–198.
132 J. F. Shin, D. C. Apperley and P. R. Slater, *Chem. Mater.*, 2010, **22**, 5945–5948.
133 K. Kakinuma, H. Yamamura and T. Atake, *J. Therm. Anal. Calorim.*, 2002, **69**, 897–904.
134 T. Hashimoto, Y. Inagaki, A. Kishi and M. Dokiya, *Solid State Ionics*, 2000, **128**, 227–231.
135 U. Matsumoto, A. Kuwabara, C. A. J. Fisher, H. Moriwake and I. Tanaka, *Phys. Chem. Chem. Phys.*, 2022, **24**, 1503–1509.
136 M. S. Islam, A. M. Nolan, S. Wang, Q. Bai, Y. Mo and Y. Mo, *Chem. Mater.*, 2020, **32**, 5028–5035.
137 L. Mazzei, F. Piccinelli, M. Bettinelli, S. F. Parker and M. Karlsson, *Solid State Ionics*, 2021, **365**, 115624.
138 S. Zhao, C. Chen, H. Li and W. Zhang, *New J. Chem.*, 2021, **45**, 4219–4226.
139 C. Navas, H. L. Tuller and H. C. Zur Loye, *J. Eur. Ceram. Soc.*, 1999, **19**, 737–740.
140 Y. Wang, K. H. Lee, H. Hyuga, H. Kita, H. Ohta and K. Koumoto, *J. Electroceramics*, 2010, **24**, 76–82.
141 S. Nuansaeng, M. Yashima, M. Matsuka and T. Ishihara, *Chem. - A Eur. J.*, 2011, **17**, 11324–11331.
142 Z. Lu, D. C. Sinclair, I. M. Reaney and X. Tan, *J. Am. Ceram. Soc.*, 2016, **99**, 515–522.
143 Y. Zhou, M. Shiraiwa, M. Nagao, K. Fujii, I. Tanaka, M. Yashima, L. Baque, J. F. Basbus, L. V. Mogni and S. J. Skinner, *Chem. Mater.*, 2021, **33**, 2139–2146.
144 H. Yaguchi, K. Fujii and M. Yashima, *J. Mater. Chem. A*, 2020, **8**, 8638–8647.
145 T. Ishihara, Y. Yan, T. Sakai and S. Ida, *Solid State Ionics*, 2016, **288**, 262–265.
146 K. Fujii and M. Yashima, *J. Ceram. Soc. Japan*, 2018, **126**, 852–859.
147 M. Shiraiwa, T. Kido, K. Fujii and M. Yashima, *J. Mater. Chem. A*, 2021, **9**, 8607–8619.
148 H. J. Stroud, C. E. Mohn, J.-A. Hernandez and N. L. Allan, *Philos. Trans. R. Soc. A Math. Phys. Eng. Sci.*, , DOI:10.1098/rsta.2020.0430.
149 G. Pasciak and J. Chmielowiec, *Adv. Appl. Ceram.*, 2021, **120**, 215–221.
150 C. K. Lee and A. R. West, *Solid State Ionics*, 1996, **86**–**88**, 235–239.

151 J. E. Auckett, K. L. Milton and I. R. Evans, *Chem. Mater.*, 2019, **31**, 1715–1719.
152 A. Gilane, S. Fop, F. Sher, R. I. Smith and A. C. McLaughlin, *J. Mater. Chem. A*, 2020, **8**, 16506–16514.
153 A. Gilane, S. Fop, D. N. Tawse, C. Ritter and A. C. McLaughlin, *Inorg. Chem.*, 2022, **61**, 1597–1602.
154 S. Fop, K. McCombie, R. I. Smith and A. C. McLaughlin, *Chem. Mater.*, 2020, **32**, 4724–4733.
155 Y. Yasui, T. Tsujiguchi, Y. Sakuda, J. R. Hester and M. Yashima, *J. Phys. Chem. C*, 2022, **126**, 2383–2393.
156 K. S. McCombie, E. J. Wildman, C. Ritter, R. I. Smith, J. M. S. Skakle and A. C. McLaughlin, *Inorg. Chem.*, 2018, **57**, 11942–11947.
157 Y. Suzuki, T. Murakami, K. Fujii, J. R. Hester, Y. Yasui and M. Yashima, *Inorg. Chem.*, 2022, 7537–7545.
158 Y. Sakuda, J. R. Hester and M. Yashima, *J. Ceram. Soc. Japan*, 2022, **130**, 442–447.
159 T. Murakami, T. Shibata, Y. Yasui, K. Fujii, J. R. Hester and M. Yashima, *Small*, 2022, **18**, 2106785.
160 M. Dion, M. Ganne and M. Tournoux, *Mater. Res. Bull.*, 1981, 16, 1429–1435.
161 A. J. Jacobson, J. W. Johnson and J. T. Lewandowski, *Inorg. Chem.*, 1985, **24**, 3727–3729.
162 E. E. Mccabe, E. Bousquet, C. P. J. Stockdale, C. A. Deacon, T. T. Tran, P. S. Halasyamani, M. C. Stennett and N. C. Hyatt, *Chem. Mater.*, 2015, **27**, 8298–8309.
163 R. J. Goff, D. Keeble, P. A. Thomas, C. Ritter, F. D. Morrison and P. Lightfoot, *Chem. Mater.*, 2009, **21**, 1296–1302.
164 T. I. Draskovic, T. Wang, C. N. Henderson and T. E. Mallouk, *Int. J. Hydrogen Energy*, 2014, **39**, 4576–4580.
165 Y. Il Kim and S. J. Kim, *Ceram. Int.*, 2015, **41**, 3318–3323.
166 J. H. Choy, J. Y. Kim, S. J. Kim, J. S. Sohn and Oc Hee Han, *Chem. Mater.*, 2001, **13**, 906–912.
167 V. Thangadurai and W. Weppner, *Solid State Ionics*, 2004, **174**, 175–183.
168 M. A. Subramanian, J. Gopalakrishnan and A. W. Sleight, *Mater. Res. Bull.*, 1988, **23**, 837–842.
169 R. J. Goff, D. Keeble, P. A. Thomas, C. Ritter, F. D. Morrison and P. Lightfoot, *Chem. Mater.*, 2009, **21**, 1296–1302.
170 V. Thangadurai and W. Weppner, *Chem. Mater.*, 2002, **14**, 1136–1143.
171 W. Zhang, K. Fujii, E. Niwa, M. Hagihala, T. Kamiyama and M. Yashima, *Nat. Commun.*, 2020, **11**, 1224.
172 W. Zhang, K. Fujii, T. Ishiyama, H. Kandabashi and M. Yashima, *J. Mater. Chem. A*, 2020, **8**, 25085–25093.
173 W. Zhang and M. Yashima, *Ceram. Int.*, 2022, **48**, 16522–16528.
174 V. A. Cascos, J. Roberts-Watts, C. Skingle, I. Levin, W. Zhang, P. S. Halasyamani, M. C. Stennett, N. C. Hyatt, E. Bousquet and E. E. McCabe, *Chem. Mater.*, 2020, **32**, 8700–8712.
175 Y.-S. Hong, S.-J. Kim, S.-J. Kim and J.-H. Choy, *J. Mater. Chem.*, 2000, **10**, 1209–1214.
176 O. H. Kwon and G. M. Choi, *Solid State Ionics*, 2006, **177**, 3057–3062.
177 K. Huang, M. Feng and J. B. Goodenough, *J. Am. Ceram. Soc.*, 1998, **81**, 357–362.
178 L. León-Reina, E. R. Losilla, M. Martínez-Lara, M. C. Martín-Sedeño, S. Bruque, P. Núñez, D. V. Sheptyakov and M. A. G. Aranda, *Chem. Mater.*, 2005, **17**, 596–600.
179 A. V. Shlyakhtina, P. Fedtke, A. Busch, I. V. Kolbanev, T. Barfels, M. Wienecke, A. E. Sokolov, V. A. Ulianov, V. A. Trounov and L. G. Shcherbakova, *Solid State Ionics*, 2008, **179**, 1004–1008.
180 S. P. Simner, D. Suarez-Sandoval, J. D. Mackenzie and B. Dunn, *J. Am. Ceram. Soc.*, 1997, **80**, 2563–2568.
181 T. Wakita and M. Yashima, *Acta Crystallogr. Sect. B Struct. Sci.*, 2007, **63**, 384–389.
182 S. Torii, M. Yonemura, T. Y. Surya Panca Putra, J. Zhang, P. Miao, T. Muroya, R. Tomiyasu, T. Morishima, S. Sato, H. Sagehashi, Y. Noda and T. Kamiyama, *J. Phys. Soc. Japan*, 2011, **80**, 3–6.
183 M. Yashima, *J. Am. Ceram. Soc.*, 2002, **85**, 2925–2930.
184 T. Wakita and M. Yashima, *Appl. Phys. Lett.*, 2008, **92**, 29–32.
185 M. Yashima, M. Itoh, Y. Inaguma and Y. Morii, *J. Am. Chem. Soc.*, 2005, **127**, 3491–3495.
186 M. Yashima and T. Tsuji, *J. Appl. Crystallogr.*, 2007, **40**, 1166–1168.

187 M. Cherry, M.S. Islam and C.R.A. Catlow, *J. Solid State Chem.*, 1995, **118**, 125–132.
188 M. Yashima and T. Kamioka, *Solid State Ionics*, 2008, **178**, 1939–1943.
189 M. Yashima, H. Yamada, S. Nuansaeng and T. Ishihara, *Chem. Mater.*, 2012, **24**, 4100–4113.
190 B. J. Kennedy, Y. Kubota, B. A. Hunter, Ismunandar and K. Kato, *Solid State Commun.*, 2003, **126**, 653–658.
191 C. H. Hervoches and P. Lightfoot, *Chem. Mater.*, 1999, **11**, 3359–3364.
192 T. W. Surta, A. Manjón-Sanz, E. K. Qian, R. H. Mansergh, T. T. Tran, L. B. Fullmer and M. R. Dolgos, *Chem. Mater.*, 2017, **29**, 7774–7784.